Evaluating Topographic Effects on Kilometer-Scale Satellite Downward Shortwave Radiation Products: A Case Study in Mid-Latitude Mountains

Yichuan Ma, Tao He, *Senior Member, IEEE*, Cristina Aguilar, Rafael Pimentel, Shunlin Liang, *Fellow, IEEE*, Tim R. McVicar, Dalei Hao, Xiongxin Xiao, and Xinyan Liu

***Abstract*— Downward shortwave radiation (DSR) is critical to many surface processes, and many satellite-derived DSR products have been released. Few studies have validated DSR over mountains where it is highly heterogeneous, and so, the shortwave flux measured at ground stations does not match kilometer-scale DSR products. To tackle this challenge, we used a high spatial resolution (30 m) daily DSR over Sierra Nevada, Spain, for 2008–2015, and a mountainous radiative transfer model to explore how topographic effects impacted the performances of DSR products. Four widely used satellite products were selected as proxies for our evaluation: 1) MCD18A1 V6.1 (with a spatial resolution of 1 km); 2) Meteosat Second Generation (MSG) DSR (∼3.3 km); 3) Global LAnd Surface Satellite (GLASS) DSR V42 (0.05°); and 4) Breathing Earth System Simulator (BESS) DSR (0.05°). There are three main findings under clear skies. First, the product accuracies were slope-dependent, decreasing by 59.8%–134.6% with a slope of ≥25° compared with areas with a slope of <10°. Second, the product accuracies were aspect-dependent, exhibiting a higher degree of overestimation (i.e., average of 27.6 W/m^2) on the north side and underestimation (i.e., an average of −1.3 W/m^2) on the south side. Third, and finally, the product accuracies were time-dependent, exhibiting seasonal variations and pronounced overestimation in summer (i.e., 8.8–18.2 W/m^2). Moreover, the impact of topography decreased with increasing cloud cover. Our findings can be applied to various mountainous areas due to the same mechanism of how topography influences the DSR estimation. This study corroborates the substantial uncertainties of the current DSR products in mountains and the necessity of incorporating topographic information into DSR estimations.**

***Index Terms*— Downward shortwave radiation (DSR), mountains, satellite products validation, topographic effect.**

Manuscript received 8 September 2023; revised 20 December 2023 and 28 January 2024; accepted 30 January 2024. Date of publication 14 February 2024; date of current version 23 February 2024. This work was supported in part by the National Key Research and Development Program of China under Grant 2020YFA0608704, in part by the National Natural Science Foundation of China under Grant 42090012, in part by the Hubei Provincial Natural Science Foundation under Grant 2021CFA082, in part by the Fundamental Research Funds for the Central Universities through Wuhan University under Grant 2042022dx0001, and in part by the Wuhan University Specific Fund for Major School-Level Internationalization Initiatives under Grant WHU-GJZDZX-RC09. The work of Yichuan Ma was supported by the China Scholarship Council. The work of Rafael Pimentel was supported in part by the Juan de la Cierva Inc. Program of the Ministry of Science and Innovation under Grant IJC2018-038093-I; and in part by the Spanish Ministry of Science and Innovation, Spanish State Research Agency, through the Severo Ochoa and María de Maeztu Program for Centers and Units of Excellence in Research and Development (a member of DAUCO, Unit of Excellence), under Grant CEX2019-000968-M. *(Corresponding author: Tao He.)*

Yichuan Ma is with Hubei Key Laboratory of Quantitative Remote Sensing of Land and Atmosphere, School of Remote Sensing and Information Engineering, Wuhan University, Wuhan 430079, China, and also with CSIRO Environment, Canberra, ACT 2601, Australia (e-mail: ma_yichuan@whu.edu.cn).

Tao He is with Hubei Key Laboratory of Quantitative Remote Sensing of Land and Atmosphere, School of Remote Sensing and Information Engineering, Wuhan University, Wuhan 430079, China (e-mail: taohers@whu.edu.cn).

Cristina Aguilar is with the Fluvial Dynamics and Hydrology Research Group, Andalusian Institute for Earth System Research (IISTA), University of Córdoba, 14071 Córdoba, Spain (e-mail: caguilar@uco.es).

Rafael Pimentel is with the Fluvial Dynamics and Hydrology Research Group, Andalusian Institute for Earth System Research (IISTA), and the Department of Agronomy, Unit of Excellence María de Maeztu (DAUCO), University of Córdoba, 14071 Córdoba, Spain (e-mail: z02piler@uco.es).

Shunlin Liang is with the Jockey Club STEM Laboratory of Quantitative Remote Sensing, Department of Geography, The University of Hong Kong, Hong Kong, China (e-mail: shunlin@hku.hk).

Tim R. McVicar is with CSIRO Environment, Canberra, ACT 2601, Australia (e-mail: tim.mcvicar@csiro.au).

Dalei Hao is with the State Key Laboratory of Remote Sensing Science, Aerospace Information Research Institute, Chinese Academy of Sciences, Beijing 100101, China (e-mail: dalei.hao@pnnl.gov).

Xiongxin Xiao is with the Institute of Geography and the Oeschger Center for Climate Change Research, University of Bern, 3012 Bern, Switzerland (e-mail: xiaoxx@whu.edu.cn).

Xinyan Liu is with the Aerospace Information Institute, Henan Academy of Sciences, Zhengzhou, China (e-mail: xinyan0712@whu.edu.cn).

Digital Object Identifier 10.1109/TGRS.2024.3365865

I. Introduction

SURFACE downward shortwave radiation (DSR) is the driving force of many land processes, such as vegetation and snow dynamics [1], [2], crop growth [3], and evapotranspiration [4], [5]. Many satellite-derived DSR products have been released [6], [7], [8] and are widely used [9], [10], [11], [12]. Furthermore, the accuracy of the DSR products has been continuously improved by upgrades to estimation algorithms [7], [13], [14], [15] and the new generation of satellites [16], [17], [18], [19].

Many evaluations of the DSR products have been conducted against shortwave flux measurements from ground networks, e.g., FLUXNET, surface radiation budget network (SURFRAD), and baseline surface radiation network [20], [21], [22], [23] where the local terrain over the evaluation sites was generally flat and homogeneous. Currently, the global DSR products can typically achieve a reasonable accuracy under most conditions (e.g., with the root-mean-square errors (RMSEs) of approximately 35 W/m^2 at daily scale [24]); however, the accuracies of the DSR products in mountainous areas have not been well documented.

Mountains cover approximately 23% of the land and are of great importance to the Earth's hydrological, ecological, social, and environmental systems [25], [26], [27]. Clear-sky DSR is abundant in mountainous areas because of their high elevation and the additional radiation reflected from surrounding environments, and accurate estimation of the DSR in mountains helps in solar energy generation [28], [29]. In addition, a better understanding of DSR patterns and variations in mountains would advance our knowledge of mountainous ecosystems and land surface processes, such as surface warming [30], vegetation dynamics [31], [32], and snow melting [33], [34]. However, the topography influences the radiative transfer over the heterogeneous land surface of mountains [35], [36], [37], [38], [39], [40], and the substantial impacts of the topography on high spatial resolution DSR (H-DSR; e.g., $\leq$100 m) estimations have been reported [41], [42], [43], [44], [45]. There is also some evidence that moderate and coarse spatial resolution (i.e., $>$100 m) shortwave radiation modeling suffers from topographic effects. For example, Liou et al. [46] found that compared with the flat surfaces, DSR anomalies on the Tibetan Plateau could reach 600 W/m^2 at a 1-km spatial scale using a 3-D Monte Carlo photon tracing program at noon. In a land surface modeling study, Hao et al. [47] incorporated subgrid topographic parameterization in the Energy Exascale Earth System Model and found that the topography could introduce the differences of $>$20 W/m^2 for 0.125° resolution net shortwave radiation at the seasonal scale on the Tibetan Plateau. However, the topographic effects on the current DSR products have typically been ignored, and the accuracies of the DSR products have not been well investigated in mountainous areas [16], [18].

In general, topography induces changes in the amount of direct and diffuse radiation the ground receives, introduces shadows, and results in the receipt of additional reflected radiation from surrounding environments. The surface heterogeneity caused by subpixel variations in the topography induces challenges in evaluating kilometer-scale DSR products in mountains. In general, there are two problems inhibiting the evaluation of the DSR products in mountains. First, ground stations in mountains are sparse, and few of them are located on sloping terrain (e.g., slope angles of greater than 5°) [48], [49], so they cannot represent the surface energy exchange scheme modified by the change in solar illumination and adjacent reflections. Second, the shortwave flux measured on the ground usually has a limited spatial footprint (e.g., decameter to hectometer scale, dependent on the local topography) and cannot match the moderate and coarse spatial resolution of DSR product pixels in mountains [50], [51]. In this context, the evaluation of the DSR products in complex mountainous areas (e.g., steep hills and valleys) remains a challenge. Nevertheless, reliable H-DSR maps could serve as a bridge to evaluate the moderate and coarse spatial resolution DSR products in mountains [52]. Nowadays, there are remaining unknowns in the performances of DSR products in mountains.

1) Are the uncertainties of DSR satellite products related to the surface heterogeneity induced by topography?
2) What factors determine the uncertainty of DSR estimation in mountains? And how?

Accordingly, we tried to answer the above two scientific questions by implementing the first comprehensive evaluation of DSR products in mountains. Our study provides instructions for the current user community, as well as recommendations for future product algorithm improvement over mountains. It should be noted that we focused on a new contribution by quantitatively assessing the contributing factors of topography to the accuracies of kilometer-scale DSR products rather than a simple evaluation of their absolute accuracies. The materials and methods are presented in Sections II and III, respectively. The evaluations of the DSR products are presented in Section IV and are discussed in Section V. Finally, the conclusions are provided in Section VI.

II. Study Area and Materials

A. Study Area

The Sierra Nevada is a typical massif of semiarid Mediterranean high mountains located in southeast Spain. Covering 2273 km^2, the Sierra Nevada contains the highest peak in continental Spain and has a large elevation variation (i.e., from 262 to 3479 m above sea level). Sierra Nevada contains a wide variety of surface topography, with a maximum slope of 50° and obvious north and south faces. There is a regular presence of snow at $>$2000 m above sea level, which may last from November to June on the summits [53]. Substantial land use and land cover types are present, including forests, urban, shrubs, crops, and pastures [54]. The diversity of topographic and ground characteristics makes Sierra Nevada a globally representative mountainous site and contributes to the better evaluation of the DSR products in this study. This study also benefits from the prevalence of clear skies in the study area [55]. Sierra Nevada has a fragile environment and has undergone substantial changes over the years [56]. Thus, it has been a scientific research hotspot, including studies focused on snow dynamics [57], [58], hydrology [59], [60], climate [61], ecosystems [62], and solar radiation [41]. Meanwhile, Sierra Nevada was internationally recognized as a biosphere reserve (2003), a national park (1999), a special area of conservation (2012), and an important observatory for global change. Fig. 1 shows the location, topography, and astronaut photograph of Sierra Nevada, Spain.

B. DSR Products

We evaluated four widely used DSR products, namely, the Moderate Resolution Imaging Spectroradiometer (MODIS) MCD18A1, Meteosat Second Generation (MSG) daily DSR flux (DIDSSF-R; hereinafter denoted as MSG DSR to make it consistent with other products), Global LAnd Surface Satellite (GLASS) DSR, and Breathing Earth System Simulator (BESS) DSR on the daily scale. Although these DSR products have been continuously improved and widely used, the topographic effects in mountains are not explicitly accounted for in their product algorithms; thus, their applicability in mountains requires further investigation. High-level information on each DSR product is shown in Table I, and detailed information is provided as follows.

1) MODIS DSR Product (MCD18A1): The MCD18A1 Version 6.1 [12] is a combined MODIS Terra and Aqua DSR gridded Level 3 product. The estimation algorithm uses

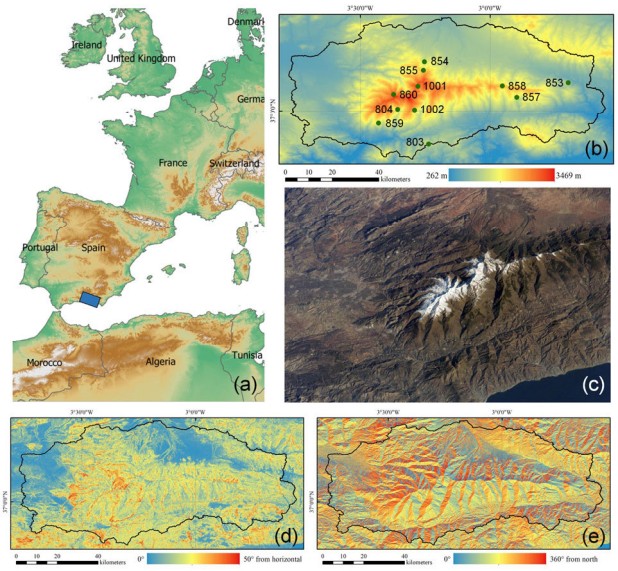

Fig. 1. Location, topography, and photograph of the Sierra Nevada, Spain. (a) Location of Sierra Nevada, Spain (marked in blue), (b) elevation distribution, and (c) astronaut photograph (acquired on December 11, 2005, with a Kodak 760C digital camera), downloaded from https://earthobservatory.nasa.gov/images/6237/sierra-nevada-spain, last accessed January 29, 2024. (d) and (e) Slope and aspect of Sierra Nevada. The DEM used for (b), (d), and (e) is AW3D30. The black lines in (b), (d), and (e) denote the study area boundary. The points in (b) refer to the ground stations for generating and evaluating H-DSR where the numbers are the station codes (for details please refer to Table B1). In (b), (d), and (e), the top-left corner is 37.3592°N, 3.7789°W; and the bottom-right corner is 36.8092°N, 2.5561°W.

TABLE I
HIGH-LEVEL INFORMATION OF THE DSR PRODUCTS EVALUATED HEREIN

Name of products	Spatial/ temporal resolutions	Temporal range	References
MCD18A1 V6.1	1 km/3 hour	Since 2000	[12]
MSG DIDSSF-R (MSG DSR)	3 km at nadir/daily	2004–2015	[63, 64]
GLASS DSR V42	0.05°/daily	2000–2020	[9]
BESS DSR	0.05°/daily	2000–2019	[11]

a lookup table (LUT), following Liang et al. [65], which directly uses top-of-atmosphere (TOA) data and does not rely on additional aerosol or cloud inputs. The MCD18A1 Version 6.1 was validated against measurements at 142 stations from six observational networks and had an RMSE of 39.2 W/m^2 at daily scale [24]. MCD18A1 has contributed to many fields, such as gross primary production estimation [66], radiative forcing quantification [67], and evaporation estimation [68]. The MCD18A1 Version 6.1 was downloaded from https://search.earthdata.nasa.gov/ (last accessed January 29, 2024), and the daily mean DSR was calculated by averaging the DSR estimates every 3 h. The MCD18A1 was also upscaled from 1 km to 0.05° (see Section III-A) for the intercomparison with GLASS DSR and BESS DSR.

2) MSG DSR Product: The MSG DSR was derived from the European Organization for the Exploitation of Meteorological Satellites (EUMETSAT) Satellite Application Facility for Land Surface Analysis (Land-SAF) [69] with observations provided by the Spinning Enhanced Visible and Infrared Imager (SEVIRI) instrument onboard the MSG series of geostationary satellites. MSG DSR was estimated with separate algorithms for clear-sky and cloudy-sky situations [63], [64]. The spatial resolution of the MSG DSR is approximately 3.3 km in our study area. MSG DSR was reported to have a standard deviation of 20–44 W/m^2 at the daily scale against six stations in Europe [63]. MSG DSR was used to map soil moisture [70], land surface temperature reconstruction [71], and topographic correction of surface reflectance [72]. We downloaded the MSG DSR from https://landsaf.ipma.pt/en/ (last accessed January 29, 2024).

3) GLASS DSR Product: The GLASS DSR V42 was generated from MODIS TOA reflectance data using a direct estimation method [9]. The GLASS DSR was validated against shortwave flux data measured at 525 ground stations around the world from 2003 to 2005, yielding an RMSE of 32.84 W/m^2 and a bias of 3.72 W/m^2 at the daily scale [9]. Studies, including energy budget generation [73], selecting photovoltaic sites [74], and long-term DSR variations analysis [2], have benefited from the GLASS DSR. We downloaded the GLASS DSR V42 product from http://glass-product.bnu.edu.cn/ (last accessed January 29, 2024).

4) BESS DSR Product: The BESS DSR was derived using an atmospheric radiative transfer model combined with an artificial neural network, and MODIS aerosol and cloud parameter products [11]. The BESS DSR has been reported to have an RMSE of 36.4 W/m^2 when validated against the same 142 stations in six observational networks as used for MCD18A1 Version 6.1 [24]. The BESS DSR has been used to explore vegetation carbon sequestration [75] and to quantify the radiative forcing of hydropower reservoirs [76]. We downloaded the BESS DSR from https://www.environment.snu.ac.kr/bess-rad (last accessed January 29, 2024).

C. Reference Data: H-DSR

We used the newly published H-DSR data across Sierra Nevada, Spain [55], as the ground truth for evaluations. The all-sky H-DSR was derived using a geographic information system (GIS)-based model [41] with topographic consideration (i.e., the hourly direct and diffuse radiation and reflected radiation from surrounding environments were modeled, and following integration daily DSR maps were ultimately obtained) driven by ground DSR measurements from weather stations, 30-m digital elevation model (DEM) data, and cloud-free Landsat images for deriving albedo [77]. The radiative transfer process has been fully accounted for in the modeling. There are many studies to evaluate DSR products using hundreds of ground-measured data, but it should be noted that they focused on the overall accuracies of the products; thus, they need globally distributed "points" to evaluate DSR products with different atmospheric conditions. However, our objective is to enhance the understanding of the topographic impacts on DSR products, and considering each pixel as a pair of evaluation, there are a total of 147 0.05° × 0.05° pairs of evaluations, which equals 4719 1×1 km pairs of evaluations covering the study area.

The locations of 11 ground stations are shown in Fig. 1(b), and detailed geolocation information is provided in Table B1. The quality of DSR observation was evaluated by Aguilar et al. [55]. The ground-measured DSR data were well quality controlled, and after the quality control, the excluded values were approximately 2% for all stations. The H-DSR used the flux data from the weather stations for interpolation, and the number of available weather stations controlled the accuracy of the H-DSR [55], so we selected the H-DSR from January 23, 2008 to December 31, 2015 (i.e., 2900 days) for evaluation, as at least seven stations were in operation then. Note that the pyranometers were horizontally set; thus, the validation of H-DSR was carried out by assuming that this pixel was a zero slope in the DEM to be able to compare with the ground-measured flux. The H-DSR has been evaluated with reliable performance, as indicated by the overall RMSE of 25.87 W/m^2 (see Fig. B1), ensuring its role as the "reference truth."

D. Topographic Data

The Advanced Land Observing Satellite (ALOS) Global Digital Surface Model "ALOS World 3D-30m (AW3D30)" has been reported the highest accuracy among the current freely available DEMs [78], [79]. We downloaded AW3D30 V3.2 from https://www.eorc.jaxa.jp/ALOS/en/dataset/aw3d30/aw3d30_e.htm (last accessed January 29, 2024) and calculated the slope, aspect (using the method of Horn [80]), and surface areas (i.e., the surface areas of pixels changes with topographic variation, by generating eight 3-D triangles connecting each pixel's center point [81]) from AW3D30 for evaluation. Although the H-DSR estimation was sensitive to DEM errors, the DSR uncertainties caused by the DEM were remarkably reduced by the spatial upscaling, i.e., the errors were less than 2% at a 3-km spatial resolution [82]. Therefore, it was reasonable to apply the state-of-the-art AW3D30 DEM to upscale the H-DSR for evaluation in this study.

III. Methods

A. Indirect Evaluation of DSR Products Over Mountains

Fig. 2(a) shows that the "point observations" by ground measurements over mountains vary substantially even within 5 km in mountains, indicating nonnegligible spatial mismatch between ground-measured DSR and kilometer-scale DSR products [52]. Thus, the previous evaluation against ground-measured data [22], [83] cannot document the topographic impacts on DSR products in mountains. Therefore, we applied H-DSR as the bridge for evaluating topographic effects in DSR products as Fig. 2(b). The evaluation was conducted mainly under clear-sky conditions to avoid the following issues under cloudy skies: 1) the mismatch between the satellite-derived DSR and ground measurements [84] and 2) the limited temporal resolution of MODIS, which makes it difficult to capture substantial cloud variations [19]. In addition, the clear-sky DSR typically suffers from greater topographic effects than cloudy skies, and thus, the evaluation of the clear-sky DSR products helps us to better understand the topographic effects on DSR estimation. The H-DSR data

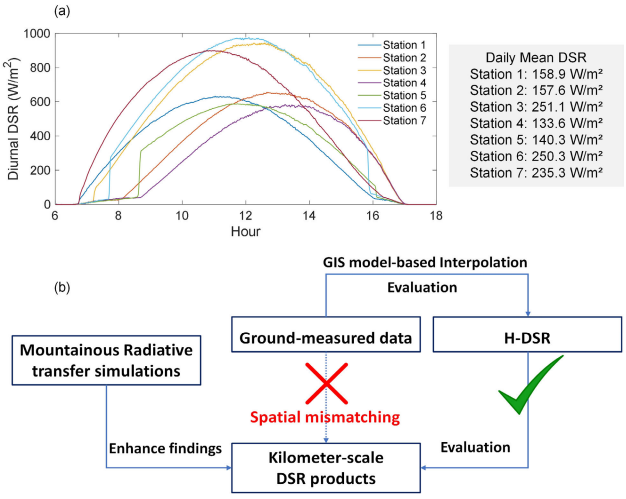

Fig. 2. Spatial heterogeneity of DSR induced by topography and strategy for evaluating topographic effects of kilometer-scale DSR products in mountains. (a) Clear-sky diurnal DSR variation and daily mean DSR over "slope-parallel" ground measurements in Chengde, China, on November 2, 2018. Note that the distances among seven stations are within 5 km, and for geolocation information, please refer to Yan et al. [52]. (b) Overall strategy for evaluation in our study. The red cross means the ground-measured data cannot be used for the evaluation of kilometer-scale DSR products in mountains because of spatial mismatching. The green tick means the H-DSR can serve as a "bridge" for the evaluation.

were validated against daily DSR measurements from weather stations in Appendix B, providing us with reliable ground-truth data for evaluating the DSR products in mountains compared with previous studies [44], [45]. In addition, given that the H-DSR errors were uniformly distributed in the study area [55], the uncertainties in the H-DSR could be largely alleviated by spatial upscaling (Fig. C1). A total of 766 clear-sky days (i.e., without any cloud contamination throughout the entire daylight period of each day) from January 23, 2008 to December 31, 2015 were selected based on the measured diurnal DSR data from weather stations in Sierra Nevada. The clearness index (CI) was calculated as the fraction of DSR and extraterrestrial radiation to separate clear sky [55]. We also visually checked the H-DSR time series to avoid cloud contamination. For the issues under cloudy-sky conditions, we also conducted the preliminary evaluation under partially cloudy (i.e., 1279 days) and fully cloudy (i.e., 814 days) conditions to explore how topography impacted DSR products under cloudy skies.

We also conducted the preliminary evaluation over Chengde, China, where the high spatial resolution daily mean DSR maps were estimated from Landsat and MODIS atmospheric product with the assumption that the atmospheric conditions were stable in the day. The integration of topography was implemented by the mountainous radiative transfer model in Section III-C. For the details of the estimation method, please refer to Ma et al. [82]. This evaluation served as an additional experiment to illustrate whether our findings remain over other areas. Besides, compared with the very limited estimation from high spatial resolution satellite data due to sparse Landsat overpass, the H-DSR generated by interpolating hourly ground measurements offered us invaluable reference data for evaluation. Note that this is a preliminary comparison, and the quantification was not conducted due to the uncertainties and assumptions

(i.e., the stable atmospheric conditions during the entire daylight hours) when estimating H-DSR from satellite data.

B. Spatial Upscaling of DSR Data

To evaluate the kilometer-scale DSR products using H-DSR (with 30-m spatial resolution), it was necessary to upscale H-DSR to spatially match DSR products. In addition, the 1-km MCD18A1 was also upscaled to 0.05° for comparison. The topography induces a difference between the surface area and projected area, so the spatial upscaling of the fluxes in mountains should include the surface area weight [85], [86]

$$E_t^{\text{coarse}} = \sum_{i=1}^{N} p_i \cdot E_{t,i}^{\text{fine}} \tag{1}$$

$$p_i = A_i \Big/ \sum_{i=1}^{N} A_i \tag{2}$$

where E_t^{coarse} and $E_{t,i}^{\text{fine}}$ are the coarse and fine spatial resolution shortwave radiation, respectively; p_i is the area-weighted ratio derived by dividing the surface area of the fine-resolution pixel by the total surface area of the coarse pixel; and A_i is the surface area of DEM pixel i derived using the method described by Jenness [81].

C. Mountainous Radiative Transfer Model

We used the mountainous radiative transfer model [37] to enhance our findings and explore the potential problems of DSR products (Sections IV-D and IV-E). The DSR in mountains includes three components, namely, direct radiation (E_t^{dir}), diffuse radiation (E_t^{dif}), and reflected radiation from the surrounding environment (E_t^{ref}), which can be calculated using the following equations, respectively:

$$E_t^{\text{dir}} = \Theta \cdot E_h^{\text{dir}} \cdot (\cos i_t / \cos \theta_s) \tag{3}$$

$$E_t^{\text{dif}} = E_h^{\text{dif}} \cdot V_d \tag{4}$$

$$E_t^{\text{ref}} = \bar{a} \cdot (1 - V_d) \cdot \left(E_h^{\text{dir}} + E_h^{\text{dif}}\right) \tag{5}$$

where Θ is the shadow factor (unitless), which is equal to 0 in shadow areas and is equal to 1 in nonshadow areas. E_h^{dir} and E_h^{dif} are the direct and diffuse radiation (W/m^2) in flat areas, respectively. θ_S is the solar zenith angle (SZA; ° from the vertical direction). V_d is the sky view factor (SVF; unitless) of the target pixel (unitless), and i_t is the local incident angle (° from the normal of terrain); the SVF and local incident angle can be derived from the DEM and solar angles [87]. $\bar{a}$ is the average surface albedo of the surrounding terrain (unitless). We assumed that the surface albedo of the targeted area was close to the average albedo of the surrounding environment: $a \approx \bar{a}$. The libRadtran 2.0.4 [88], [89] was used to drive the mountainous radiative transfer simulations: the direct and diffuse radiation can be obtained by setting SZA, atmospheric parameters, and surface albedo. For details about how TOA reflectance is modeled in the mountainous radiative transfer model, please see Ma et al. [37].

The objective of employing the mountainous radiative transfer model is twofold: 1) to investigate whether neglecting topography results in time-varying deviations in regional DSR estimation and 2) to elucidate the reasons behind the overestimations observed in the evaluation of MCD18A1. For the first goal, simulations of both DSR with and without topographic consideration were conducted over Sierra Nevada, Spain, on four solar points to quantify regional deviations. The simulations encompassed various combinations of aerosol optical depth (AOD; 0.2 and 0.4) and albedo (0.2 and 0.6) to represent distinct atmosphere and surface conditions. It is worth noting that AOD and surface albedo were selected as variables due to their crucial impacts on clear-sky DSR. For the second goal, as MCD18A1 utilizes blue-band TOA reflectance data to determine atmospheric optical depth, simulations of blue-band TOA reflectance were performed over both rugged terrain and flat areas under clear-sky and cloudy-sky conditions. A comparative analysis was conducted to assess the differences between them. The simulation parameters included an SZA of 60°, a view zenith angle of 0°, and an elevation of 2 km. Clear-sky conditions ranged from AOD = 0, 0.05, 0.10, 0.15, 0.20, 0.30, 0.4, and 0.6, while cloudy-sky conditions varied in terms of cloud optical depth (COD) from 1, 3, 5, 10, 30, 40, 50, 60, 70, 80, and 100. The sloping terrain had a local incidence angle of 30° and an SVF of 0.93. A spectral library containing 245 typical surface spectra [37], [90], [91] of snow, vegetation, and soil was used.

IV. Results

A. Preliminary Comparison of the H-DSR and DSR Products

Fig. 3 shows the DSR patterns of the H-DSR (at the 30-m spatial resolution), upscaled H-DSR with the spatial resolutions of 1 km and 0.05°, MCD18A1, MSG DSR, GLASS DSR, and BESS DSR around three solar points (i.e., the two solstices and the autumnal equinox, and the spring equinox was not shown since the similar DSR pattern as the autumnal equinox). Fig. 3 clearly shows that topographic effects are substantial for the 30-m H-DSR. The DSR varied with the topography for the upscaled H-DSR (i.e., spatial resolutions of 1 km and 0.05°), yet the MCD18A1, MSG DSR, GLASS DSR, and BESS DSR values were very homogeneous over the study area. Moreover, the MCD18A1 had some underestimations on the summits, especially during the winter equinox, compared with the H-DSR and other DSR products. Fig. 4 further shows the function of the spatial resolution and temporal variations on the DSR values based on the H-DSR and upscaled H-DSR at four solar points. The DSR ranges at the two equinoxes were similar, since the clear-sky DSR largely depended on the SZA. The H-DSR on December 22, 2008 varied from 0.0 to 322.4 W/m^2 at a spatial resolution of 30 m, from 24.8 to 254.6 W/m^2 at 1 km, and from 87.6 to 182.3 W/m^2 at 0.05°. Note that the minimum H-DSR is about 0.042 before rounding on December 22, 2008, and the close to zero value could be attributed to the sheltering effects from surrounding mountains during the whole day. On June 21, 2012, the H-DSR varied from 138.2 to 418.7 W/m^2 at a spatial resolution of 30 m, from 260.5 to 400.3 W/m^2 at 1 km, and from 301.8 to 371.4 W/m^2 at 0.05°. This is consistent with our knowledge that topographic effects generally decrease with increasing pixel size [92] and increase with increasing SZA (i.e., from summer to winter) [37], [39].

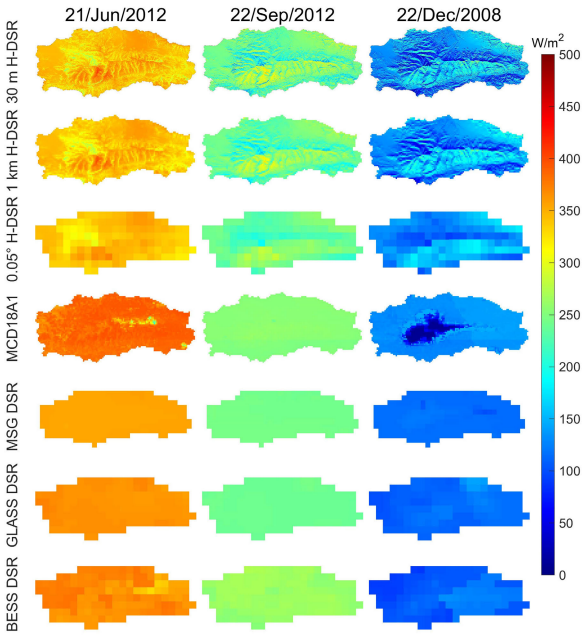

Fig. 3. Clear-sky H-DSR (30 m), upscaled H-DSR with the spatial resolutions of 1 km and 0.05°, MCD18A1 (1 km), MSG DSR (approximately 3.3 km), GLASS DSR (0.05°), and BESS DSR (0.05°) around three solar points (i.e., the two solstices and the autumnal equinox). The specific date is noted at the top of the column.

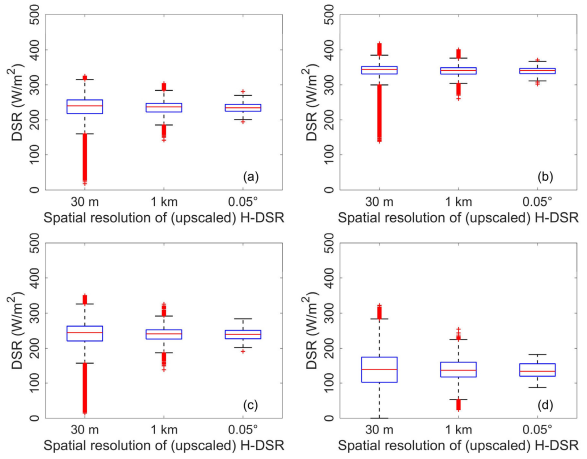

Fig. 4. Boxplot of the clear-sky DSR ranges for the H-DSR (30 m) and upscaled H-DSR with the spatial resolution of 1 km and 0.05° around four solar points (i.e., the two solstices and two equinoxes). Evaluations on (a) March 22, 2008, (b) June 21, 2012, (c) September 22, 2012, and (d) December 22, 2008.

Fig. A1 shows the comparison using the satellite-derived H-DSR in Chengde, China. We only obtained three entire clear-sky images (with no clouds in the whole daylight time) from 2013 to 2019 because of the high cloud cover and sparse overpassing of Landsat 8. There was an overestimation of H-DSR on June 1, 2017 [82], so it exhibited higher values than the three DSR products. In general, the comparison offers the same information as Fig. 3 that the kilometer-scale DSR products are homogenous and do not show variations with topography, while the topographic impacts exist even for the upscaled H-DSR at 0.05° resolution.

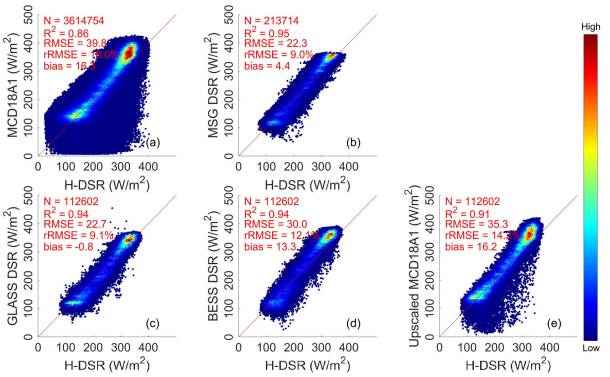

Fig. 5. Overall evaluation of the clear-sky daily mean (a) MCD18A1 (1 km), (b) MSG DSR (approximately 3.3 km), (c) GLASS DSR (0.05°), (d) BESS DSR (0.05°), and (e) upscaled MCD18A1 (0.05°) against the H-DSR over Sierra Nevada from January 23, 2008 to December 31, 2015. N is the sample size. The RMSE and bias have the units of W/m^2. The colors indicate the relative data density.

B. Overall Evaluation Accuracies

We conducted an overall evaluation of the MCD18A1 (1 km), MSG DSR (approximately 3.3 km), GLASS DSR (0.05°), BESS DSR (0.05°), and upscaled MCD18A1 (0.05°) against the H-DSR in Sierra Nevada. Fig. 5 shows the overall evaluation of the daily mean clear-sky DSR from January 23, 2008 to December 31, 2015. As can be seen from Fig. 5, the R^2, RMSE, relative RMSE (rRMSE), and bias of the MCD18A1 were 0.86, 39.8 W/m^2, 16.0%, and 16.3 W/m^2, respectively, and those of the MSG DSR were 0.95, 22.3 W/m^2, 9.0%, and 4.4 W/m^2, respectively. The GLASS DSR achieved an R^2 of 0.94, an RMSE of 22.7 W/m^2, an rRMSE of 9.1%, and a bias of -0.8 W/m^2, while the BESS DSR achieved the values of 0.94, 30.0 W/m^2, 12.1%, and 13.3 W/m^2, respectively. With spatial upscaling from 1 km to 0.05°, the accuracy of the MCD18A1 improved (R^2 = 0.91, RMSE = 35.3 W/m^2, rRMSE = 14.2%, and bias = 16.2 W/m^2), yet the upscaled MCD18A1 still performed worse than the GLASS and BESS DSR. The MCD18A1 contained substantial underestimations in Fig. 5(a) where the maximum deviation reached 345.7 W/m^2, and the upscaling alleviated this issue.

Fig. 6 shows the pixel-scale evaluation results for the MCD18A1, MSG DSR, GLASS DSR, BESS DSR, and upscaled MCD18A1 in Sierra Nevada. The RMSE and bias exhibited considerable heterogeneity in the study area, especially for the MCD18A1 at >2000 m above sea level (Fig. 1). The RMSE of the MCD18A1 ranged from 17.4 to 137.9 W/m^2, and the bias ranged from -91.2 to 99.0 W/m^2. The MCD18A1 performed better with upscaling, with the RMSE values of 17.2–83.4 W/m^2 and the bias values of -52.8 to 42.1 W/m^2. The performances of the MSG DSR, GLASS DSR, and BESS DSR were more stable than those of the MCD18A1. The RMSE of the MSG DSR ranged from 10.6 to 54.6 W/m^2, and the bias ranged from -28.2 to 52.3 W/m^2; the GLASS DSR had the RMSE values of 12.2–42.6 W/m^2 and the bias values of -30.2 to 37.6 W/m^2; the BESS DSR had the RMSE values of 19.2–54.1 W/m^2 and the bias values of -18.8 to 50.0 W/m^2. Despite the remarkable differences in the performances of these DSR products, their

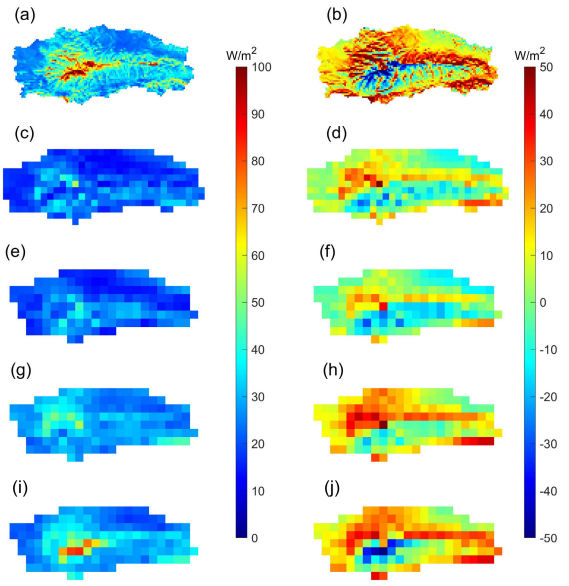

Fig. 6. RMSE and bias patterns of the MCD18A1 (1 km), MSG DSR (approximately 3.3 km), GLASS DSR (0.05°), BESS DSR (0.05°), and upscaled MCD18A1 (0.05°). RMSEs of (a) MCD18A1, (c) MSG DSR, (e) GLASS DSR, (g) BESS DSR, and (i) upscaled MCD18A1, which share the same color bar. Biases of (b) MCD18A1, (d) MSG DSR, (f) GLASS DSR, (h) BESS DSR, and (j) upscaled MCD18A1, which share the same color bar.

RMSE and bias patterns were similar, with the following: 1) larger RMSEs in the rugged terrain than in the flat areas (Fig. 1) and 2) positive biases (i.e., overestimation) in the northern Sierra Nevada and underestimation in the southern Sierra Nevada.

C. Evaluating the Topographic Effects on DSR Products

To investigate how topography impacted the DSR products, we conducted further evaluations of the four DSR products under different terrain conditions. Table II shows the evaluations of the DSR products for different slope ranges. The low uncertainties of the four DSR products compared with the H-DSR in flat areas (i.e., a slope of $<10°$) demonstrated the consistency of the DSR products with the H-DSR for relatively smooth terrain and highlighted the fact that the poor performances of the DSR products in the rugged terrain (Fig. 6) were related to the topography. All DSR products showed worse performances with increasing slope (from slope $<10°$ to $\geq 25°$), i.e., the RMSE increased by 134.6% (from 24.3 to 57.0 W/m^2) for the MCD18A1, 86.5% (from 16.3 to 30.4 W/m^2) for the MSG DSR, 59.8% (from 18.4 to 29.4 W/m^2) for the GLASS DSR, and 62.4% (from 25.0 to 40.6 W/m^2) for the BESS DSR. We also explored how topography impacted the evaluation results under cloudy-sky conditions (Fig. D1). The performances of the DSR products did not typically depend on the topography under fully cloudy conditions, yet the performances of the DSR products deteriorated with increasing slopes under partially cloudy conditions, while the variations were much lower than those under clear skies.

Fig. 7 shows the evaluations of the DSR products for the south- and north-facing slopes, where pixels with slope angles $\geq 10°$ were included. The MSG DSR and GLASS DSR had larger RMSEs on the south-facing slope (24.8 and 26.1 W/m^2, respectively) than on the north-facing slope (22.6 and 20.2 W/m^2, respectively). However, the RMSEs of the MCD18A1 and BESS DSR were lower on the south-facing slopes (40.8 and 29.1 W/m^2, respectively) than on the north-facing slopes (44.8 and 32.6 W/m^2, respectively). In addition, substantial differences in the bias were observed on the south- and north-facing slopes; that is, the DSR products all showed overestimation on the north-facing slopes (i.e., from 10.1 to 33.5 W/m^2) and a small or negative bias on the south-facing slopes (i.e., from -9.2 to 7.1 W/m^2). The difference in the bias between the north- and south-facing slopes within a certain satellite product ranged from 18.1 W/m^2 (MSG DSR) to 29.8 W/m^2 (MCD18A1). The evaluation in this section showed that the topography, in terms of both the slope and aspect of the terrain, largely determined the performances of the DSR products in mountains.

TABLE II

EVALUATION OF THE DAILY MEAN CLEAR-SKY MCD18A1 (1 KM), MSG DSR (APPROXIMATELY 3.3 KM), GLASS DSR (0.05°), BESS DSR (0.05°), AND UPSCALED MCD18A1 (0.05°) AGAINST THE H-DSR FOR DIFFERENT SLOPE RANGES FROM JANUARY 23, 2008 TO DECEMBER 31, 2015. THE RMSE AND BIAS HAVE THE UNITS OF W/M^2. THE [0, 10) FOR SLOPE MEANS THE PIXELS WHERE SLOPE ANGLES ARE $\geq 0°$ AND $<10°$, AND SO ON FOR THE OTHER CLASSES

Slope (°)	R^2	RMSE	rRMSE	bias
MCD18A1				
[0, 10)	0.96	24.3	9.5%	12.6
[10, 15)	0.93	29.0	11.5%	13.7
[15, 20)	0.88	36.2	14.2%	11.6
[20, 25)	0.83	43.6	17.7%	17.2
>=25	0.75	57.0	24.6%	28.9
MSG DSR				
[0, 10)	0.98	16.3	6.4%	-1.7
[10, 15)	0.97	18.3	7.4%	4.5
[15, 20)	0.95	21.8	8.7%	2.6
[20, 25)	0.94	24.0	9.7%	4.8
>=25	0.94	30.4	13.0%	19.9
GLASS DSR				
[0, 10)	0.97	18.4	7.2%	–5.4
[10, 15)	0.97	17.7	7.1%	–1.6
[15, 20)	0.95	21.2	8.5%	–1.4
[20, 25)	0.93	24.9	10.0%	–0.6
>=25	0.92	29.4	12.4%	10.3
BESS DSR				
[0, 10)	0.97	25.0	9.9%	9.1
[10, 15)	0.96	25.2	10.1%	12.3
[15, 20)	0.95	28.2	11.4%	12.8
[20, 25)	0.92	31.6	12.7%	13.1
>=25	0.91	40.6	17.1%	24.9
Upscaled MCD18A1				
[0, 10)	0.96	24.6	9.7%	13.7
[10, 15)	0.96	27.3	10.9%	17.8
[15, 20)	0.94	31.8	12.8%	18.3
[20, 25)	0.87	39.8	16.0%	14.3
>=25	0.83	48.4	20.4%	21.0

D. Exploration of the Time-Varying Deviations in DSR Products

In this section, we explored whether there are time-varying deviations in the DSR products resulting from the topography.

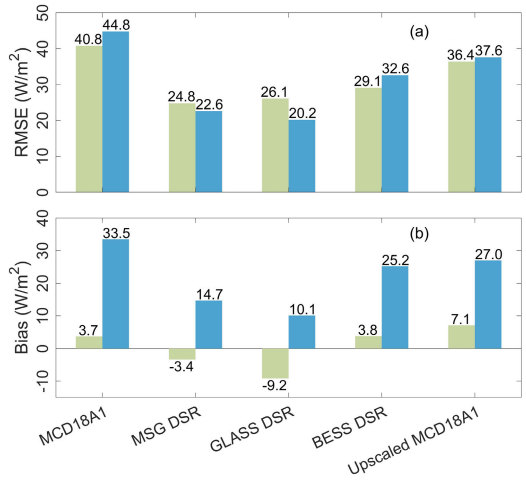

Fig. 7. Evaluation of the daily mean clear-sky DSR products against the H-DSR on the south-facing slope (green bars) and the north-facing slope (blue bars) from January 23, 2008 to December 31, 2015. The pixels with the slope angles of $\geq 10°$ are countered. (a) RMSE and (b) bias of DSR products. Parts (a) and (b) share the same X-axis.

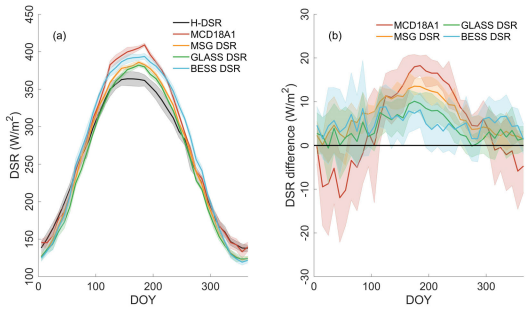

Fig. 8. Variations in the clear-sky DSR with DOY for the H-DSR and the four DSR products with DOY. (a) Variation of clear-sky DSR with DOY in Sierra Nevada. (b) DSR difference between the four products and the H-DSR between the complex terrain (i.e., the slope of $\geq 10°$) and the relatively flat terrain (i.e., the slope of $<10°$) with DOY in Sierra Nevada. The line refers to the mean DSR values or the mean DSR difference calculated using a moving ten-day interval in each year, and the shading represents the standard deviation.

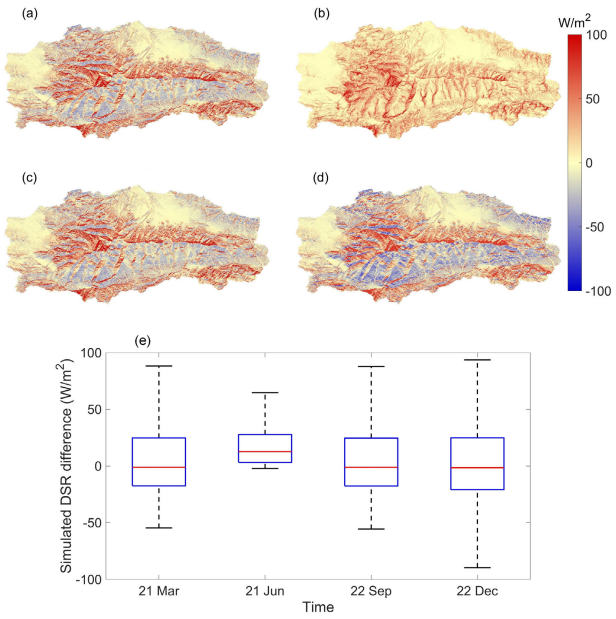

Fig. 9. Overall mean simulated DSR difference (i.e., simulated DSR without topography minus simulated DSR with topography) at four solar points. (a)–(d) Pixel-scale mean simulated DSR differences at four solar points. Simulated DSR difference on (a) March 21, (b) June 21, (c) September 22, and (d) December 22. (e) Boxplot of the simulated DSR differences at four solar points. The simulations include four conditions with the combination of AOD = 0.2 and 0.4 and surface albedo = 0.2 and 0.6.

Here, we utilized day of year (DOY) as the proxy for evaluating whether the performance of DSR products is time-dependent. Fig. 8(a) shows the variations in the clear-sky DSR with DOY based on the H-DSR and four DSR products. Fig. 8(b) shows the DSR difference between each of the four DSR products and the H-DSR between the complex terrain and relatively flat terrain (e.g., DSR difference for MCD18A1 = (MCD18A1_complex − H-DSR_complex) − (MCD18A1_flat − H-DSR_flat), where "_complex" and "_flat" refer to the areas with the slopes of $\geq 10°$ and the areas with the slopes of $<10°$, respectively), indicating the deviation of the DSR products caused by the topography. The general tendency of the variations in the DSR with DOY is consistent with our knowledge that the DSR is higher in summer and lower in winter. The MSG DSR, GLASS DSR, and BESS DSR showed overestimations compared with the H-DSR during summer and limited discrepancies in winter, with the DSR differences of −0.5 to 13.6 W/m^2 for the MSG DSR, −1.1 to 10.1 W/m^2 for the GLASS DSR, and 1.4–8.8 W/m^2 for the BESS DSR. However, the MCD18A1 exhibited underestimations related to the unstable estimations (the DSR difference ranged from −12.0 to 18.2 W/m^2), and we further investigate this issue in Section IV-E.

We also conducted a radiative transfer simulation (see Section III-C) to demonstrate whether ignoring the topography contributed to the time-varying deviations of the DSR products. Fig. 9 shows the overall mean simulated DSR differences (i.e., simulated DSR without topography minus simulated DSR with topography) at the four solar points over Sierra Nevada. The dependence of the DSR on the terrain aspect increased from summer to winter when the topography was ignored (i.e., overestimation on the north-facing slopes and underestimation on the south-facing slopes). The DSR difference was typically positive (i.e., overestimation of the DSR when the topography was ignored) in summer when the overall mean DSR difference reached 18.8 W/m^2 (relative difference = 5.0%), and the overestimation decreased from summer to winter (i.e., mean DSR differences of 7.8 W/m^2 (3.1%) at the fall equinox and 3.3 W/m^2 (2.9%) at the winter solstice). This is consistent with the overall trends in Fig. 8.

E. Exploration of MCD18A1's Potential Problems

Based on the previous results, in this section, we explore the potential problems with the MCD18A1 in mountains, specifically the unsatisfactory underestimations (Figs. 3 and 5). Fig. 10 shows the examples of unsatisfactory underestimations in MCD18A1, and Fig. 11 shows the corresponding spatial upscaled H-DSR (1 km) for comparison. The MCD18A1 does not incorporate topographic consideration, so the estimated DSR is supposed to generally remain homogeneous over the entire Sierra Nevada, but underestimation occurred with a

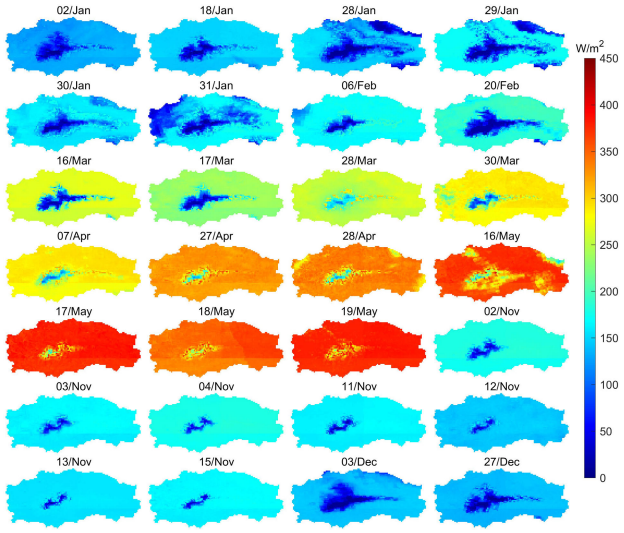

Fig. 10. Examples of unsatisfactory underestimations in MCD18A1 in 2010. The labels are the date of the MCD18A1.

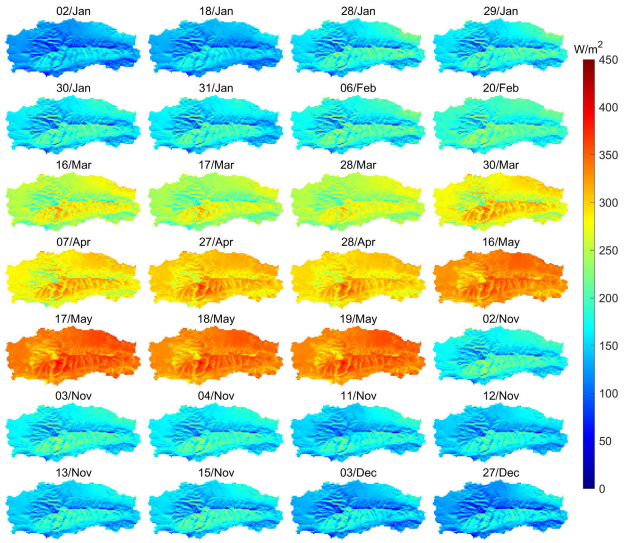

Fig. 11. Spatial upscaled H-DSR (1 km) for comparison with the MCD18A1 in Fig. 10. The labels are the date of upscaled H-DSR in 2010.

high frequency. From Figs. 10 and 11, we primarily found that the unsatisfactory underestimations exhibit certain spatial and temporal patterns: 1) they mostly occur in winter and spring (i.e., DOY 1–120 and 305–365) and 2) they have approximately similar spatial coverages and typically occur in high-elevation areas (Fig. 1).

We used the mountainous radiative transfer model (see Section III-C) to explore the potential mechanisms for this issue. We compared the difference between the clear-sky and cloudy-sky blue-band TOA reflectance, because the MCD18A1 uses the blue-band (MODIS band 3) TOA reflectance to determine the atmospheric optical depth. Fig. 12 shows the range of the simulated blue-band clear-sky and cloudy-sky TOA reflectance in the flat areas and specific terrain areas with an SZA equal to 60°. In the flat areas, the difference between the simulated clear-sky and cloudy-sky

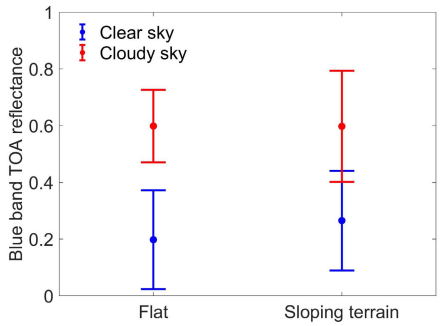

Fig. 12. Range of simulated clear-sky and cloudy-sky blue band TOA reflectance variations over the flat areas and specific sloping terrain. SZA= 60°, view zenith angle = 0°, and elevation = 2 km. The clear skies have AOD = 0, 0.05, 0.10, 0.15, 0.20, 0.30, 0.4, and 0.6; the cloudy skies have COD = 1, 3, 5, 10, 30, 40, 50, 60, 70, 80, and 100. The sloping terrain has a local incidence angle of 30° and an SVF of 0.93. Dots refer to the mean TOA reflectance, and the bars denote one standard deviation for each condition.

blue-band TOA reflectance was obvious (i.e., higher blue-band TOA reflectance in cloudy sky and lower values in clear sky), while the topography impacted TOA reflectance, and the ranges of the clear-sky and cloudy-sky TOA reflectance overlapped in the specific terrain areas. Specifically, the blue-band TOA reflectance-based atmospheric optical depth retrieval method could separate cloudy pixels and clear pixels over flat areas, yet it was difficult to do so with topographic effects.

V. Discussion

A. Topographic Effects on DSR Products

Yan et al. [52] evaluated the MCD18A1 and Himawari-8 DSR in a 5 × 5 km area and found that they were stable (i.e., RMSE = 41.254 and 61.707 W/m^2 for 3-h scale MCD18A1 and 1-h scale Himawari-8, respectively). Jin et al. [50] also found that the 1-h scale GLASS DSR achieved a satisfactory performance (RMSE = 81.91 W/m^2) compared with fine spatial resolution DSR maps. According to Figs. 7 and 8, the specific topographic and temporal conditions controlled the DSR evaluation results; thus, our results do not contradict those of previous studies, and a comprehensive evaluation under diverse topographic and temporal conditions is needed.

Although the four DSR products we evaluated were based on different estimation strategies (see Section II-B), they exhibited similar influences from topography, e.g., the accuracies decreased with increasing slope (Table II). The impacts of the topography resulted in different DSR patterns according to (3)–(5), for example, lower DSR on the north-facing slopes (i.e., terrain away from the sun in the northern hemisphere) and higher DSR on the south-facing slopes (i.e., terrain facing the sun in the northern hemisphere). This resulted in overestimations on the north-facing slopes and underestimation on the south-facing slopes when topographic effects were ignored (Fig. 7) at around 37°N of Sierra Nevada. Besides, the obstruction induced by the mountains on sensor observations could contribute uncertainties in DSR estimation over mountains [86]. Our results are consistent with those of previous studies; that is, the topography affected the kilometer-scale shortwave radiation modeling [47], [93], though the topographic effects decreased with upscaling (Figs. 3 and 4).

B. Time-Varying Deviations of DSR Products in Mountains

Several studies have presented large differences in DSR between mountains and flat areas [86], [92], [94]. How topography controls the instantaneous DSR at the pixel scale can be seen from (3)–(5): under clear-sky conditions, the direct radiation dominates, and the DSR achieves higher values for the terrain facing the sun (i.e., smaller local incidence angles) and lower values for the terrain away from the sun or in shadowed areas. However, how topography impacts the daily mean DSR at the regional scale has largely remained unclear. From Figs. 8 and 9, we observed the time-varying deviations of the mean DSR in Sierra Nevada when ignoring topographic effects from both satellite products and mountainous radiative transfer simulations. We obtained possible explanations for why large DSR overestimations occurred in summer. The daily mean DSR mainly depended on the local incidence angle (i.e., SZA for flat areas) around local noon under clear-sky conditions, while at noon in summer, most of the pixels might have local incidence angles larger than their SZA. For example, when the SZA was 15° at local noon, most of the pixels in mountains did not have such small solar incidence angles, and thus, the direct radiation over the sloping terrain was less than that over the flat terrain. In addition, due to the long daylight duration in summer, the variation in the sun azimuth angle (SAA) was large, and thus, few pixels were always facing the sun, resulting in a smaller daily mean DSR in mountains and an overestimation of the DSR when ignoring topography. In contrast, the pixels were continuously facing toward or away from the sun during the day in winter because of the relatively large SZA and small variation in the SAA within a day. Meanwhile, the radiation reflected from the surrounding snow-covered areas enhanced the local DSR in winter [95]. Thus, the regional DSR pattern that ignored the topography in winter differed from that in summer (Fig. 9): most of the pixels in summer showed overestimations of DSR when ignoring topography, while the simulated DSR difference was more symmetric in winter. Noting that this phenomenon is related to the variation of solar angle and, thus, geolocation-dependent. The deviations of cloud-sky DSR depended more on the atmospheric conditions, e.g., the diffuse radiation dominated the DSR under thick clouds, and the mountains resulted in shelters of DSR in mountains, thus overestimation of DSR when topographic effects were ignored [37]. Gu et al. [96] also found that the simulated summer mean DSR decreased by more than 30 W/m^2 in the southern and western Tibetan Plateau when topographic considerations were integrated. In general, the current DSR products lead to time-varying deviations at the regional scale, inducing issues in studies on dimming and brightening [97], snow dynamics evaluation [98], gross primary production [99], evaporation [100], and surface warming [101].

C. Additional Issues and Future Study

Our evaluation results were somewhat impacted by the geolocation errors of the DSR products [102]. However, our primary conclusions persist because of the relatively homogeneous values of the clear-sky DSR products (Fig. 3). The various surface and topographic characteristics in Sierra Nevada (Section II-A), ensured the universality of our results. Our findings can also be extended to other areas because of the same mechanism by which the topography influences the DSR [see (3)–(5)]. The preliminary comparison in Appendix A showed that the low temporal resolution of high spatial resolution satellite data and the difficulty of temporal extrapolation from instantaneous estimation to daily mean DSR limited the application of satellite estimation for DSR products evaluation in mountains. This indicated that the H-DSR used in this study offered an invaluable chance to understand the topographic effects in mountains.

According to Figs. 3 and 5, substantial underestimations occurred in the MCD18A1. From Figs. 10 and 11 as well as previous studies [103], the underestimations may be related to snow. Li et al. [24] reported that the misclassification of bright surfaces and clouds based on the blue band introduces uncertainties in the MCD18A1. We found that the topography made it difficult to distinguish clear sky and cloudy sky using the blue-band TOA reflectance data (Fig. 12), thus resulting in misestimation of atmospheric optical depth (e.g., the clear-sky snow-covered sloping terrain was misestimated as high COD), ultimately introducing substantial underestimations into the DSR estimation results. The performances of the other DSR products were reasonable, presumably because of the following: 1) more spectral bands were used (i.e., GLASS DSR) or atmospheric parameter products were inputted (i.e., the MSG DSR and BESS DSR), which helped to better separate the clear-sky and cloudy-sky data, and 2) the coarser spatial resolution of the data alleviated the impacts of topography.

In addition to the accuracies of the DSR products being slope-dependent, aspect-dependent, and time-dependent (Sections IV-C and IV-D), the result of our study indicates that additional issues may be introduced into DSR products when topographic effects are ignored, and our results highlight the necessity of integrating topographic consideration into DSR generation. For future updates of the DSR products, we recommend incorporating two key points relating to topography: 1) the sun-target-sensor geometry changes in complex terrain, so the impact of the topography on satellite observations should be considered [86], [102] and 2) the mountains typically experience high cloud dynamics [104], so integrating topographic consideration under cloudy-sky conditions is necessary (see Fig. D1 and Ma et al. [37]).

VI. Conclusion

This is the first comprehensive assessment of how topography impacts the performances of DSR products in mountains. We evaluated the MCD18A1, MSG DSR, GLASS DSR, and BESS DSR products using the H-DSR as the ground-truth data in Sierra Nevada, Spain, a typical mid-latitude massif with mountains. The mountainous radiative transfer simulations were applied to demonstrate our findings. Overall, the topographic conditions substantially controlled the accuracies of the DSR products. We concluded that the performances of the clear-sky DSR products in mountains were slope-dependent, aspect-dependent, and time-dependent.

1) With increasing slope (from <10° to ≥25°), the RMSE increased by 134.6% (24.3–57.0 W/m^2) for the MCD18A1, 86.5% (16.3–30.4 W/m^2) for the MSG DSR, 59.8% (18.4–29.4 W/m^2) for the GLASS DSR, and 62.4% (25.0–40.6 W/m^2) for the BESS DSR.
2) The four DSR products all exhibited relative overestimation on the north-facing slopes (i.e., 10.1–33.5 W/m^2) and underestimation on the south-facing slopes (i.e., −9.2 to 7.1 W/m^2) compared with their bias values in the flat areas (i.e., −5.4 to 12.6 W/m^2) in the northern hemisphere. This would be reversed beyond the tropics in the southern hemisphere.
3) The DSR products did not perform equally among the different temporal ranges, and the selected DSR products all produced overestimations in summer (i.e., 8.8–18.2 W/m^2), and the discrepancies decreased from summer to winter.
4) The cloudy-sky DSR also suffered from topographic effects, yet the topographic effects decreased with cloud cover increased. We found that there were unexpected uncertainties in the current DSR products in mountains, and we demonstrated the necessity of integrating topographic considerations into DSR estimations. Owing to the same mechanism of how topographic effects impact DSR estimation, our findings can be further extended to various mountainous areas. We highlight the fact that the current DSR products should be carefully considered before being applied in mountainous areas.

APPENDIX

A. Preliminary Evaluation of DSR Products in Chengde, China

Fig. A1 shows the comparison of H-DSR derived from satellite estimation [82], the upscaled DSR, and the DSR products. Note that MSG DSR is geostationary satellite-based data, and it is not available in China.

B. Evaluation of H-DSR Against Ground-Measured Flux

We conducted the evaluation of H-DSR against ground-measured flux following Aguilar et al. [55]. Note that the slight differences in the validation results compared with Aguilar et al. [55] were attributed to the update of H-DSR and different temporal periods for evaluation. The geolocation information of ground measurements is provided in Table B1. The performance of H-DSR was reasonable under clear-sky conditions (i.e., overall RMSE = 25.87 W/m^2) and deteriorated with more clouds (Fig. B1).

C. Uncertainties of H-DSR on DSR Evaluation

Although the H-DSR has been reported to have high accuracy under clear-sky conditions, uncertainties remain in the H-DSR and are presumably from DEM errors, resampling errors, and algorithm uncertainties. We introduced 10% random error (refer to Aguilar et al. [55]) into the H-DSR to investigate how the uncertainties impacted DSR evaluation in our study. Fig. C1 shows the impact of the 10% random errors on the 1-km DSR and 0.05° DSR. The uncertainties were largely reduced by the upscaling, and the maximum RMSEs were 1.4 and 0.9 W/m^2 for the 1-km and 0.05° spatial resolutions, respectively.

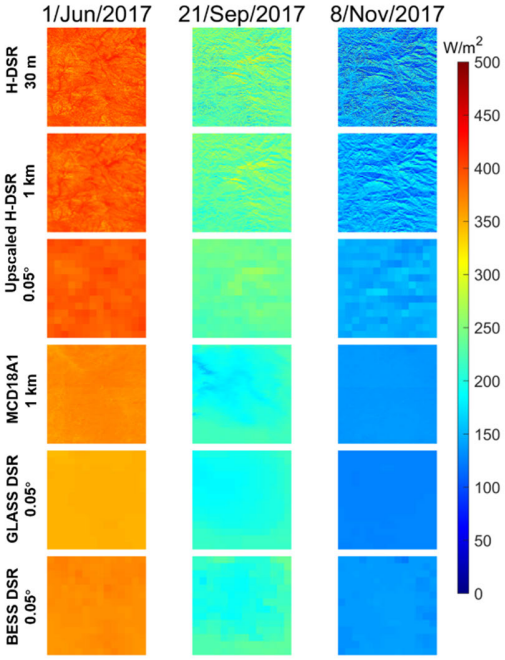

Fig. A1. Clear-sky H-DSR (30 m), upscaled H-DSR with the spatial resolutions of 1 km and 0.05°, MCD18A1 (1 km), GLASS DSR (0.05°), and BESS DSR (0.05°) for three days with clear-sky conditions. Each column refers to the DSR at the same solar points, and the specific date is noted at the top of the column. The top-left corner is 41.8°N, 118.0°E; and the bottom-right corner is 41.1°N, 118.7°E.

TABLE B1
GEOLOCATION INFORMATION OF THE GROUND MEASUREMENTS USED FOR H-DSR GENERATION AND EVALUATION

Station code	Elevation/m	Latitude/°	Longitude/°
803	1332	36.871	-3.237
804	2141	37.007	-3.356
853	975	37.110	-2.699
854	1530	37.191	-3.253
855	2155	37.158	-3.257
857	1732	37.054	-2.897
858	2300	37.098	-2.953
859	1735	36.952	-3.430
860	3097	37.065	-3.372
1001	2867	37.096	-3.278
1002	2325	37.004	-3.291

D. Evaluation Under Partially Cloudy and Fully Cloudy Conditions

A total of 1279 partially cloudy conditions and 814 fully cloudy condition data were finally selected based on both the ground-measured data and the H-DSR patterns (see Section II-C). Fig. D1 shows the evaluation of the DSR products for different slope ranges under partially cloudy and fully cloudy conditions. The RMSE typically increased with increasing cloud cover. For partially cloudy conditions, the RMSEs of the four DSR products generally increased

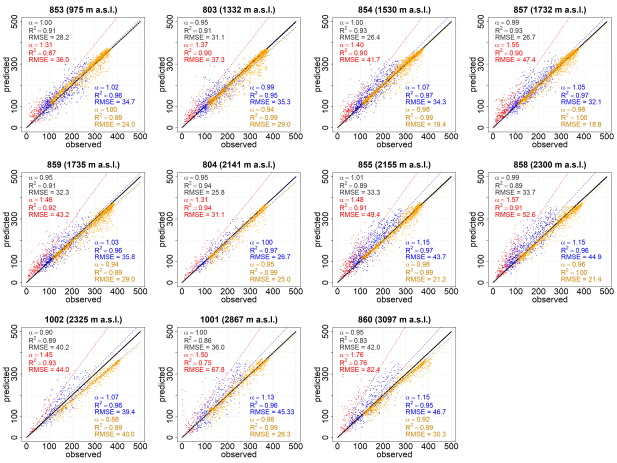

Fig. B1. Cross validation of H-DSR against ground-measured shortwave flux. Linear fits of daily predicted versus observed DSR at each of the selected stations for all data (black) and cloudy (CI < 0.3—red), partly cloudy (0.3 < CI < 0.6—blue), and clear-sky (CI > 0.6—orange) days. The black numbers above each subplot are the station code (see Fig. 1(b) for locations) and elevation. For all subplots, the solid black line is the 1:1 line, and lines of best fit for all data and the three cloudy classes are provided in the relevant color on each subplot. Units of all axes are W/m^2. The subplots are ordered by site elevation, starting from the top left, by row, to the bottom right.

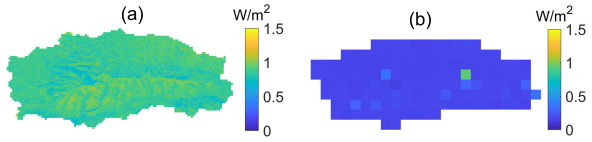

Fig. C1. Impact of the 10% random error in the 30-m clear-sky H-DSR on (a) overall mean RMSE of the 1-km DSR and (b) overall mean RMSE of the 0.05° DSR. Please refer to Fig. 1 for the geolocation information.

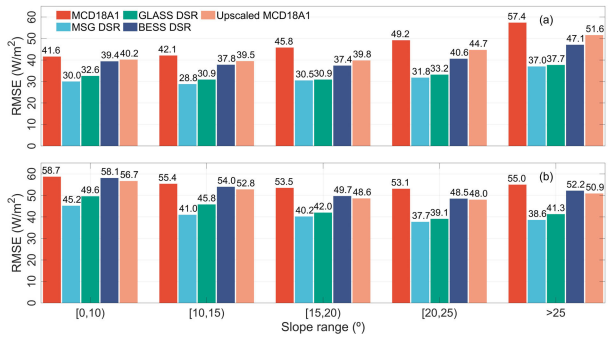

Fig. D1. RMSE of the daily mean DSR products against the H-DSR under (a) partially full and (b) fully cloudy conditions on varying slopes. (a) and (b) Share the same X-axis and legend. The [0, 10) for the slope range means the pixels had the slope angles of $\geq 0°$ and $<10°$, and so on for the other X-axis groupings. Parts (a) and (b) share the same X-axis.

with increasing slope, i.e., the RMSE increased from 41.6 to 57.4 W/m^2 (RMSE increased by 38.0%) for the MCD18A1, 30.0 to 37.0 W/m^2 (23.3%) for the MSG DSR, 32.6 to 37.7 W/m^2 (15.6%) for the GLASS DSR, and 39.4 to 47.1 (19.5%) W/m^2 for the BESS DSR in the areas with the slopes of $<10°$ to $\geq 25°$. The performances of the four DSR products did not show obvious dependence on the slope under fully cloudy conditions.

ACKNOWLEDGMENT

The authors would like to thank the NASA Moderate Resolution Imaging Spectroradiometer (MODIS) Land Science Team for providing MCD18A1 data; the European Organization for the Exploitation of Meteorological Satellites (EUMETSAT) Satellite Application Facility for Land Surface Analysis (Land-SAF) for providing Meteosat Second Generation (MSG) daily DSR flux (DIDSSF-R) data; the Environmental Ecology Laboratory, Seoul National University, for providing Breathing Earth System Simulator (BESS) downward shortwave radiation (DSR) data; Beijing Normal University for providing Global LAnd Surface Satellite (GLASS) DSR data; and Japan's Aerospace Exploration Agency for providing AW3D30 digital elevation model (DEM). They would also like to thank the journal editorial team and the four anonymous reviewers for constructive critical comments, which were the catalyst for improvement of our research.

REFERENCES

[1] F. Comola et al., "Scale-dependent effects of solar radiation patterns on the snow-dominated hydrologic response," *Geophys. Res. Lett.*, vol. 42, no. 10, pp. 3895–3902, May 2015, doi: 10.1002/2015gl064075.

[2] S. Chen et al., "Vegetation structural change and CO_2 fertilization more than offset gross primary production decline caused by reduced solar radiation in China," *Agricult. Forest Meteorol.*, vol. 296, Jan. 2021, Art. no. 108207, doi: 10.1016/j.agrformet.2020.108207.

[3] Y. Fan et al., "Solar geoengineering can alleviate climate change pressures on crop yields," *Nature Food*, vol. 2, no. 5, pp. 373–381, May 2021, doi: 10.1038/s43016-021-00278-w.

[4] R. J. Donohue, T. R. McVicar, and M. L. Roderick, "Assessing the ability of potential evaporation formulations to capture the dynamics in evaporative demand within a changing climate," *J. Hydrol.*, vol. 386, nos. 1–4, pp. 186–197, May 2010, doi: 10.1016/j.jhydrol.2010.03.020.

[5] Z. Xie et al., "The global LAnd surface satellite (GLASS) evapotranspiration product version 5.0: Algorithm development and preliminary validation," *J. Hydrol.*, vol. 610, Jul. 2022, Art. no. 127990, doi: 10.1016/j.jhydrol.2022.127990.

[6] D. Hao et al., "DSCOVR/EPIC-derived global hourly and daily downward shortwave and photosynthetically active radiation data at 0.1° *times* 0.1° resolution," *Earth Syst. Sci. Data*, vol. 12, no. 3, pp. 2209–2221, Sep. 2020, doi: 10.5194/essd-12-2209-2020.

[7] R. Li, D. Wang, S. Liang, A. Jia, and Z. Wang, "Estimating global downward shortwave radiation from VIIRS data using a transfer-learning neural network," *Remote Sens. Environ.*, vol. 274, Jun. 2022, Art. no. 112999, doi: 10.1016/j.rse.2022.112999.

[8] W. Tang, K. Yang, J. Qin, X. Li, and X. Niu, "A 16-year dataset (2000–2015) of high-resolution (3 h, 10 km) global surface solar radiation," *Earth Syst. Sci. Data*, vol. 11, no. 4, pp. 1905–1915, Dec. 2019, doi: 10.5194/essd-11-1905-2019.

[9] X. Zhang et al., "An operational approach for generating the global land surface downward shortwave radiation product from MODIS data," *IEEE Trans. Geosci. Remote Sens.*, vol. 57, no. 7, pp. 4636–4650, Jul. 2019, doi: 10.1109/TGRS.2019.2891945.

[10] K.-G. Karlsson et al., "CLARA-a2: The second edition of the CM SAF cloud and radiation data record from 34 years of global AVHRR data," *Atmos. Chem. Phys.*, vol. 17, no. 9, pp. 5809–5828, May 2017, doi: 10.5194/acp-17-5809-2017.

[11] Y. Ryu, C. Jiang, H. Kobayashi, and M. Detto, "MODIS-derived global land products of shortwave radiation and diffuse and total photosynthetically active radiation at 5 km resolution from 2000," *Remote Sens. Environ.*, vol. 204, pp. 812–825, Jan. 2018, doi: 10.1016/j.rse.2017.09.021.

[12] D. Wang, S. Liang, Y. Zhang, X. Gao, M. G. L. Brown, and A. Jia, "A new set of MODIS land products (MCD18): Downward shortwave radiation and photosynthetically active radiation," *Remote Sens.*, vol. 12, no. 1, p. 168, Jan. 2020, doi: 10.3390/rs12010168.

[13] Y. Zhang, T. He, S. Liang, D. Wang, and Y. Yu, "Estimation of all-sky instantaneous surface incident shortwave radiation from moderate resolution imaging spectroradiometer data using optimization method," *Remote Sens. Environ.*, vol. 209, pp. 468–479, May 2018, doi: 10.1016/j.rse.2018.02.052.

[14] H. Jiang, N. Lu, J. Qin, W. Tang, and L. Yao, "A deep learning algorithm to estimate hourly global solar radiation from geostationary satellite data," *Renew. Sustain. Energy Rev.*, vol. 114, Oct. 2019, Art. no. 109327, doi: 10.1016/j.rser.2019.109327.

[15] W. Leng et al., "All-sky surface and top-of-atmosphere shortwave radiation components estimation: Surface shortwave radiation, PAR, UV radiation, and TOA albedo," *Remote Sens. Environ.*, vol. 298, Dec. 2023, Art. no. 113830, doi: 10.1016/j.rse.2023.113830.

[16] H. Letu et al., "A review of the estimation of downward surface shortwave radiation based on satellite data: Methods, progress and problems," *Sci. China, Earth Sci.*, vol. 63, no. 6, pp. 774–789, Jun. 2020, doi: 10.1007/s11430-019-9589-0.

[17] H. Letu et al., "High-resolution retrieval of cloud microphysical properties and surface solar radiation using Himawari-8/AHI next-generation geostationary satellite," *Remote Sens. Environ.*, vol. 239, Mar. 2020, Art. no. 111583, doi: 10.1016/j.rse.2019.111583.

[18] G. Huang et al., "Estimating surface solar irradiance from satellites: Past, present, and future perspectives," *Remote Sens. Environ.*, vol. 233, Nov. 2019, Art. no. 111371, doi: 10.1016/j.rse.2019.111371.

[19] D. Hao et al., "Estimating hourly land surface downward shortwave and photosynthetically active radiation from DSCOVR/EPIC observations," *Remote Sens. Environ.*, vol. 232, Oct. 2019, Art. no. 111320, doi: 10.1016/j.rse.2019.111320.

[20] X. Zhang, S. Liang, M. Wild, and B. Jiang, "Analysis of surface incident shortwave radiation from four satellite products," *Remote Sens. Environ.*, vol. 165, pp. 186–202, Aug. 2015, doi: 10.1016/j.rse.2015.05.015.

[21] R. Urraca et al., "Extensive validation of CM SAF surface radiation products over Europe," *Remote Sens. Environ.*, vol. 199, pp. 171–186, Sep. 2017, doi: 10.1016/j.rse.2017.07.013.

[22] K. Yang et al., "Evaluation of satellite estimates of downward shortwave radiation over the Tibetan Plateau," *J. Geophys. Res., Atmos.*, vol. 113, no. D17, Sep. 2008, Art. no. D17204, doi: 10.1029/2007jd009736.

[23] L. Tong, T. He, Y. Ma, and X. Zhang, "Evaluation and intercomparison of multiple satellite-derived and reanalysis downward shortwave radiation products in China," *Int. J. Digit. Earth*, vol. 16, no. 1, pp. 1853–1884, Oct. 2023, doi: 10.1080/17538947.2023.2212918.

[24] R. Li, D. Wang, and S. Liang, "Comprehensive assessment of five global daily downward shortwave radiation satellite products," *Sci. Remote Sens.*, vol. 4, Dec. 2021, Art. no. 100028, doi: 10.1016/j.srs.2021.100028.

[25] W. W. Immerzeel et al., "Importance and vulnerability of the world's water towers," *Nature*, vol. 577, no. 7790, pp. 364–369, Jan. 2020, doi: 10.1038/s41586-019-1822-y.

[26] M. J. Steinbauer et al., "Accelerated increase in plant species richness on mountain summits is linked to warming," *Nature*, vol. 556, no. 7700, pp. 231–234, Apr. 2018, doi: 10.1038/s41586-018-0005-6.

[27] S. B. Rumpf et al., "From white to green: Snow cover loss and increased vegetation productivity in the European Alps," *Science*, vol. 376, no. 6597, pp. 1119–1122, Jun. 2022, doi: 10.1126/science.abn6697.

[28] L. Xu, E. Long, J. Wei, Z. Cheng, and H. Zheng, "A new approach to determine the optimum tilt angle and orientation of solar collectors in mountainous areas with high altitude," *Energy*, vol. 237, Dec. 2021, Art. no. 121507, doi: 10.1016/j.energy.2021.121507.

[29] A. Kahl, J. Dujardin, and M. Lehning, "The bright side of PV production in snow-covered mountains," *Proc. Nat. Acad. Sci. USA*, vol. 116, no. 4, pp. 1162–1167, Jan. 2019, doi: 10.1073/pnas.1720808116.

[30] N. Pepin et al., "Elevation-dependent warming in mountain regions of the world," *Nature Climate Change*, vol. 5, no. 5, pp. 424–430, May 2015, doi: 10.1038/nclimate2563.

[31] J. Bian, A. Li, G. Lei, Z. Zhang, and X. Nan, "Global high-resolution mountain green cover index mapping based on Landsat images and Google Earth engine," *ISPRS J. Photogramm. Remote Sens.*, vol. 162, pp. 63–76, Apr. 2020, doi: 10.1016/j.isprsjprs.2020.02.011.

[32] G. Yin et al., "Aspect matters: Unraveling microclimate impacts on mountain greenness and greening," *Geophys. Res. Lett.*, vol. 50, no. 24, Dec. 2023, Art. no. e2023GL105879, doi: 10.1029/2023gl105879.

[33] C. Sarangi et al., "Dust dominates high-altitude snow darkening and melt over high-mountain Asia," *Nature Climate Change*, vol. 10, no. 11, pp. 1045–1051, Nov. 2020, doi: 10.1038/s41558-020-00909-3.

[34] X. Xiao, T. Zhang, X. Zhong, and X. Li, "Spatiotemporal variation of snow depth in the northern Hemisphere from 1992 to 2016," *Remote Sens.*, vol. 12, no. 17, p. 2728, Aug. 2020, doi: 10.3390/rs12172728.

[35] S. Sandmeier and K. I. Itten, "A physically-based model to correct atmospheric and illumination effects in optical satellite data of rugged terrain," *IEEE Trans. Geosci. Remote Sens.*, vol. 35, no. 3, pp. 708–717, May 1997.

[36] F. Li et al., "A physics-based atmospheric and BRDF correction for Landsat data over mountainous terrain," *Remote Sens. Environ.*, vol. 124, pp. 756–770, Sep. 2012, doi: 10.1016/j.rse.2012.06.018.

[37] Y. Ma et al., "Estimation of fine spatial resolution all-sky surface net shortwave radiation over mountainous terrain from Landsat 8 and Sentinel-2 data," *Remote Sens. Environ.*, vol. 285, Feb. 2023, Art. no. 113364, doi: 10.1016/j.rse.2022.113364.

[38] J. Wen et al., "Estimating surface BRDF/albedo over rugged terrain using an extended multisensor combined BRDF inversion (EMCBI) model," *IEEE Geosci. Remote Sens. Lett.*, vol. 19, pp. 1–5, 2022, doi: 10.1109/LGRS.2022.3143197.

[39] Y. Xian, T. Wang, W. Cheng, H. Letu, Y. Du, and W. Leng, "A uniform model for correcting shortwave downward radiation over rugged terrain at various scales," *IEEE Trans. Geosci. Remote Sens.*, vol. 61, 2023, Art. no. 5610812, doi: 10.1109/TGRS.2023.3278081.

[40] H. Liang, B. Jiang, J. Peng, S. Li, J. Han, and X. Yin, "Estimating daily surface downward shortwave radiation over rugged terrain without bright surface at 30 m on clear-sky days using CERES data," *Int. J. Digit. Earth*, vol. 16, no. 2, pp. 4317–4345, Dec. 2023, doi: 10.1080/17538947.2023.2263421.

[41] C. Aguilar, J. Herrero, and M. J. Polo, "Topographic effects on solar radiation distribution in mountainous watersheds and their influence on reference evapotranspiration estimates at watershed scale," *Hydrol. Earth Syst. Sci.*, vol. 14, no. 12, pp. 2479–2494, Dec. 2010, doi: 10.5194/hess-14-2479-2010.

[42] Y. L. Zhang, X. Li, and Y. Bai, "An integrated approach to estimate shortwave solar radiation on clear-sky days in rugged terrain using MODIS atmospheric products," *Solar Energy*, vol. 113, pp. 347–357, Mar. 2015, doi: 10.1016/j.solener.2014.12.028.

[43] M. Olson and S. Rupper, "Impacts of topographic shading on direct solar radiation for valley glaciers in complex topography," *Cryosphere*, vol. 13, no. 1, pp. 29–40, Jan. 2019, doi: 10.5194/tc-13-29-2019.

[44] N. Helbig, H. L'we, B. Mayer, and M. Lehning, "Explicit validation of a surface shortwave radiation balance model over snow-covered complex terrain," *J. Geophys. Res., Atmos.*, vol. 115, no. D18, Sep. 2010, Art. no. D18113, doi: 10.1029/2010jd013970.

[45] W. Wang, G. Yin, W. Zhao, F. Wen, and D. Yu, "Spatial downscaling of MSG downward shortwave radiation product under clear-sky condition," *IEEE Trans. Geosci. Remote Sens.*, vol. 58, no. 5, pp. 3264–3272, May 2020, doi: 10.1109/TGRS.2019.2951699.

[46] K. N. Liou, W.-L. Lee, and A. Hall, "Radiative transfer in mountains: Application to the Tibetan Plateau," *Geophys. Res. Lett.*, vol. 34, no. 23, Dec. 2007, Art. no. L23809, doi: 10.1029/2007gl031762.

[47] D. Hao, G. Bisht, Y. Gu, W.-L. Lee, K.-N. Liou, and L. R. Leung, "A parameterization of sub-grid topographical effects on solar radiation in the E3SM land model (version 1.0): implementation and evaluation over the Tibetan Plateau," *Geoscientific Model Develop.*, vol. 14, no. 10, pp. 6273–6289, Oct. 2021, doi: 10.5194/gmd-14-6273-2021.

[48] G. Pastorello et al., "The FLUXNET2015 dataset and the ONEFlux processing pipeline for eddy covariance data," *Scientific Data*, vol. 7, no. 1, p. 225, Jul. 2020, doi: 10.1038/s41597-020-0534-3.

[49] Y. Ma et al., "Landsat snow-free surface albedo estimation over sloping terrain: Algorithm development and evaluation," *IEEE Trans. Geosci. Remote Sens.*, vol. 60, 2022, Art. no. 4408914, doi: 10.1109/TGRS.2022.3149762.

[50] H.-A. Jin et al., "Validation of global land surface satellite (GLASS) downward shortwave radiation product in the rugged surface," *J. Mountain Sci.*, vol. 10, no. 5, pp. 812–823, Oct. 2013, doi: 10.1007/s11629-013-2543-6.

[51] J. Wen et al., "Validation of the MCD43A3 collection 6 and GLASS V04 snow-free albedo products over rugged terrain," *IEEE Trans. Geosci. Remote Sens.*, vol. 60, 2022, Art. no. 5632311, doi: 10.1109/TGRS.2022.3214103.

[52] G. Yan et al., "An operational method for validating the downward shortwave radiation over rugged terrains," *IEEE Trans. Geosci. Remote Sens.*, vol. 59, no. 1, pp. 714–731, Jan. 2021, doi: 10.1109/TGRS.2020.2994384.

[53] M. J. Polo et al., "Snow dynamics, hydrology, and erosion," in *The Landscape of the Sierra Nevada: A Unique Laboratory of Global Processes in Spain*, R. Zamora and M. Oliva, Eds., Cham, Switzerland: Springer, 2022, pp. 149–164.

[54] R. Moreno-Llorca, A. S. Vaz, J. Herrero, A. Millares, F. J. Bonet-García, and D. Alcaraz-Segura, "Multi-scale evolution of ecosystem services' supply in sierra Nevada (Spain): An assessment over the last half-century," *Ecosystem Services*, vol. 46, Dec. 2020, Art. no. 101204, doi: 10.1016/j.ecoser.2020.101204.

[55] C. Aguilar, R. Pimentel, and M. J. Polo, "Two decades of distributed global radiation time series across a mountainous semiarid area (Sierra Nevada, Spain)," *Earth Syst. Sci. Data*, vol. 13, no. 3, pp. 1335–1359, Mar. 2021, doi: 10.5194/essd-13-1335-2021.

[56] M. Oliva, J. M. Fernández-Fernández, and J. Martín-Díaz, "The geographic uniqueness of the Sierra Nevada in the context of the mid-latitude mountains," in *The Landscape Sierra Nevada*. Cham, Switzerland: Springer, 2022, pp. 3–9.

[57] J. Herrero and M. J. Polo, "Evaposublimation from the snow in the Mediterranean mountains of sierra Nevada (Spain)," *Cryosphere*, vol. 10, no. 6, pp. 2981–2998, Dec. 2016, doi: 10.5194/tc-10-2981-2016.

[58] R. Pimentel, J. Herrero, Y. Zeng, Z. Su, and M. J. Polo, "Study of snow dynamics at subgrid scale in semiarid environments combining terrestrial photography and data assimilation techniques," *J. Hydrometeorology*, vol. 16, no. 2, pp. 563–578, Apr. 2015, doi: 10.1175/jhm-d-14-0046.1.

[59] E. Pastén-Zapata et al., "The effect of weighting hydrological projections based on the robustness of hydrological models under a changing climate," *J. Hydrol., Regional Stud.*, vol. 41, Jun. 2022, Art. no. 101113, doi: 10.1016/j.ejrh.2022.101113.

[60] E. Contreras, J. Herrero, L. Crochemore, C. Aguilar, and M. J. Polo, "Seasonal climate forecast skill assessment for the management of water resources in a run of river hydropower system in the poqueira river (Southern Spain)," *Water*, vol. 12, no. 8, p. 2119, Jul. 2020, doi: 10.3390/w12082119.

[61] M. Pérez-Palazón, R. Pimentel, and M. Polo, "Climate trends impact on the snowfall regime in Mediterranean mountain areas: Future scenario assessment in sierra Nevada (Spain)," *Water*, vol. 10, no. 6, p. 720, Jun. 2018, doi: 10.3390/w10060720.

[62] R. Zamora et al., "Global change impact in the sierra Nevada long-term ecological research site (Southern Spain)," *Bull. Ecological Soc. Amer.*, vol. 98, no. 2, pp. 157–164, Apr. 2017, doi: 10.1002/bes2.1308.

[63] B. Geiger, C. Meurey, D. Lajas, L. Franchistéguy, D. Carrer, and J.-L. Roujean, "Near real-time provision of downwelling shortwave radiation estimates derived from satellite observations," *Meteorological Appl.*, vol. 15, no. 3, pp. 411–420, 2008, doi: 10.1002/met.84.

[64] D. Carrer et al., "Land surface albedo and down-welling shortwave radiation retrievals using high frequency observations from MSG geostationary satellite," in *Proc. IGARSS IEEE Int. Geosci. Remote Sens. Symp.*, vol. 5, Jul. 2008, pp. V-487–V-490, doi: 10.1109/IGARSS.2008.4780135.

[65] S. Liang, T. Zheng, R. Liu, H. Fang, S. Tsay, and S. Running, "Estimation of incident photosynthetically active radiation from moderate resolution imaging spectrometer data," *J. Geophys. Res., Atmos.*, vol. 111, no. D15, Aug. 2006, Art. no. D15208, doi: 10.1029/2005jd006730.

[66] W. Wu, H. E. Epstein, H. Guo, X. Li, and C. Gong, "A pigment ratio index based on remotely sensed reflectance provides the potential for universal gross primary production estimation," *Environ. Res. Lett.*, vol. 16, no. 5, May 2021, Art. no. 054065, doi: 10.1088/1748-9326/abf3dc.

[67] T. Guo, T. He, S. Liang, J.-L. Roujean, Y. Zhou, and X. Huang, "Multi-decadal analysis of high-resolution albedo changes induced by urbanization over contrasted Chinese cities based on Landsat data," *Remote Sens. Environ.*, vol. 269, Feb. 2022, Art. no. 112832, doi: 10.1016/j.rse.2021.112832.

[68] J. Zhang et al., "Spatiotemporal variations of evapotranspiration in Amazonia using the wavelet phase difference analysis," *J. Geophys. Res., Atmos.*, vol. 127, no. 10, May 2022, Art. no. e2021JD034959, doi: 10.1029/2021jd034959.

[69] I. F. Trigo et al., "The satellite application facility for land surface analysis," *Int. J. Remote Sens.*, vol. 32, no. 10, pp. 2725–2744, May 2011, doi: 10.1080/01431161003743199.

[70] Y. Wang, P. Leng, J. Ma, and J. Peng, "A method for downscaling satellite soil moisture based on Land Surface Temperature and net surface shortwave radiation," *IEEE Geosci. Remote Sens. Lett.*, vol. 19, pp. 1–5, 2022, doi: 10.1109/LGRS.2021.3062453.

[71] W. Zhao and S.-B. Duan, "Reconstruction of daytime land surface temperatures under cloud-covered conditions using integrated MODIS/Terra land products and MSG geostationary satellite data," *Remote Sens. Environ.*, vol. 247, Sep. 2020, Art. no. 111931, doi: 10.1016/j.rse.2020.111931.

[72] W. Zhao, X. Li, W. Wang, F. Wen, and G. Yin, "DSRC: An improved topographic correction method for optical remote-sensing observations based on surface downwelling shortwave radiation," *IEEE Trans. Geosci. Remote Sens.*, vol. 60, 2022, Art. no. 5606015, doi: 10.1109/TGRS.2021.3083754.

[73] Y. Wang et al., "Surface shortwave net radiation estimation from Landsat TM/ETM+ data using four machine learning algorithms," *Remote Sens.*, vol. 11, no. 23, p. 2847, Nov. 2019. [Online]. Available: https://www.mdpi.com/2072-4292/11/23/2847

[74] S. Wang, L. Zhang, D. Fu, X. Lu, T. Wu, and Q. Tong, "Selecting photovoltaic generation sites in Tibet using remote sensing and geographic analysis," *Sol. Energy*, vol. 133, pp. 85–93, Aug. 2016, doi: 10.1016/j.solener.2016.03.069.

[75] Y. Chen et al., "Accelerated increase in vegetation carbon sequestration in China after 2010: A turning point resulting from climate and human interaction," *Global Change Biol.*, vol. 27, no. 22, pp. 5848–5864, Nov. 2021, doi: 10.1111/gcb.15854.

[76] G. Wohlfahrt, E. Tomelleri, and A. Hammerle, "The albedo–climate penalty of hydropower reservoirs," *Nature Energy*, vol. 6, no. 4, pp. 372–377, Feb. 2021, doi: 10.1038/s41560-021-00784-y.

[77] R. Pimentel, J. Herrero, and M. J. Polo, "Estimating snow albedo patterns in a Mediterranean site from Landsat TM and ETM+ images," in *Proc. SPIE*, 2013, Art. no. 88870L.

[78] J. J. Carrera-Hernández, "Not all DEMs are equal: An evaluation of six globally available 30 m resolution DEMs with geodetic benchmarks and LiDAR in Mexico," *Remote Sens. Environ.*, vol. 261, Aug. 2021, Art. no. 112474, doi: 10.1016/j.rse.2021.112474.

[79] K. Liu, C. Song, L. Ke, L. Jiang, Y. Pan, and R. Ma, "Global open-access DEM performances in Earth's most rugged region high mountain Asia: A multi-level assessment," *Geomorphology*, vol. 338, pp. 16–26, Aug. 2019, doi: 10.1016/j.geomorph.2019.04.012.

[80] B. K. P. Horn, "Hill shading and the reflectance map," *Proc. IEEE*, vol. 69, no. 1, pp. 14–47, 1981, doi: 10.1109/proc.1981.11918.

[81] J. S. Jenness, "Calculating landscape surface area from digital elevation models," *Wildl. Soc. Bull.*, vol. 32, no. 3, pp. 829–839, 2004, doi: 10.2193/0091-7648(2004)032[0829:CLSAFD]2.0.CO;2.

[82] Y. Ma, T. He, S. Liang, and X. Xiao, "Quantifying the impacts of DEM uncertainty on clear-sky surface shortwave radiation estimation in typical mountainous areas," *Agricult. Forest Meteorol.*, vol. 327, Dec. 2022, Art. no. 109222, doi: 10.1016/j.agrformet.2022.109222.

[83] Y. Ryu, S. Kang, S.-K. Moon, and J. Kim, "Evaluation of land surface radiation balance derived from Moderate Resolution Imaging Spectroradiometer (MODIS) over complex terrain and heterogeneous landscape on clear sky days," *Agricult. Forest Meteorol.*, vol. 148, no. 10, pp. 1538–1552, Sep. 2008, doi: 10.1016/j.agrformet.2008.05.008.

[84] Y. Qin, T. R. McVicar, J. Huang, S. West, and A. D. L. Steven, "On the validity of using ground-based observations to validate geostationary-satellite-derived direct and diffuse surface solar irradiance: Quantifying the spatial mismatch and temporal averaging issues," *Remote Sens. Environ.*, vol. 280, Oct. 2022, Art. no. 113179, doi: 10.1016/j.rse.2022.113179.

[85] G. Yan, T. Wang, Z. Jiao, X. Mu, J. Zhao, and L. Chen, "Topographic radiation modeling and spatial scaling of clear-sky land surface longwave radiation over rugged terrain," *Remote Sens. Environ.*, vol. 172, pp. 15–27, Jan. 2016, doi: 10.1016/j.rse.2015.10.026.

[86] T. Wang, G. Yan, X. Mu, Z. Jiao, L. Chen, and Q. Chu, "Toward operational shortwave radiation modeling and retrieval over rugged terrain," *Remote Sens. Environ.*, vol. 205, pp. 419–433, Feb. 2018, doi: 10.1016/j.rse.2017.11.006.

[87] J. Dozier and J. Frew, "Rapid calculation of terrain parameters for radiation modeling from digital elevation data," *IEEE Trans. Geosci. Remote Sens.*, vol. 28, no. 5, pp. 963–969, Sep. 1990, doi: 10.1109/36.58986.

[88] C. Emde et al., "The libRadtran software package for radiative transfer calculations (version 2.0.1)," *Geosci. Model Develop.*, vol. 9, no. 5, pp. 1647–1672, May 2016, doi: 10.5194/gmd-9-1647-2016.

[89] B. Mayer and A. Kylling, "Technical note: The libRadtran software package for radiative transfer calculations–description and examples of use," *Atmos. Chem. Phys.*, vol. 5, no. 7, pp. 1855–1877, Jul. 2005, doi: 10.5194/acp-5-1855-2005.

[90] J. Chen, T. He, and S. Liang, "Estimation of daily all-wave surface net radiation with multispectral and multitemporal observations from GOES-16 ABI," *IEEE Trans. Geosci. Remote Sens.*, vol. 60, 2022, Art. no. 4407916, doi: 10.1109/TGRS.2022.3140335.

[91] T. He, S. Liang, D. Wang, Q. Shi, and M. L. Goulden, "Estimation of high-resolution land surface net shortwave radiation from AVIRIS data: Algorithm development and preliminary results," *Remote Sens. Environ.*, vol. 167, pp. 20–30, Sep. 2015, doi: 10.1016/j.rse.2015.03.021.

[92] H. Shi and Z. Xiao, "Exploring topographic effects on surface parameters over rugged terrains at various spatial scales," *IEEE Trans. Geosci. Remote Sens.*, vol. 60, 2022, Art. no. 4404616, doi: 10.1109/TGRS.2021.3098607.

[93] W.-L. Lee, K. N. Liou, and C.-C. Wang, "Impact of 3-D topography on surface radiation budget over the Tibetan Plateau," *Theor. Appl. Climatol.*, vol. 113, nos. 1–2, pp. 95–103, Jul. 2013, doi: 10.1007/s00704-012-0767-y.

[94] N. Helbig and H. Löwe, "Shortwave radiation parameterization scheme for subgrid topography," *J. Geophys. Res., Atmos.*, vol. 117, no. D3, Feb. 2012, Art. no. D03112, doi: 10.1029/2011jd016465.

[95] Q. Chu et al., "Quantitative analysis of terrain reflected solar radiation in snow-covered mountains: A case study in Southeastern Tibetan Plateau," *J. Geophys. Res., Atmos.*, vol. 126, no. 11, Jun. 2021, Art. no. e2020JD034294, doi: 10.1029/2020jd034294.

[96] C. Gu et al., "The wet bias of RegCM4 over Tibet Plateau in summer reduced by adopting the 3D sub-grid terrain solar radiative effect parameterization scheme," *J. Geophys. Res., Atmos.*, vol. 127, no. 21, Nov. 2022, Art. no. e2022JD037434, doi: 10.1029/2022jd037434.

[97] M. Wild, S. Wacker, S. Yang, and A. Sanchez-Lorenzo, "Evidence for clear-sky dimming and brightening in central Europe," *Geophys. Res. Lett.*, vol. 48, no. 6, Mar. 2021, Art. no. e2020GL092216, doi: 10.1029/2020gl092216.

[98] M. Girona-Mata, E. S. Miles, S. Ragettli, and F. Pellicciotti, "High-resolution snowline delineation from Landsat imagery to infer snow cover controls in a Himalayan catchment," *Water Resour. Res.*, vol. 55, no. 8, pp. 6754–6772, Aug. 2019, doi: 10.1029/2019wr024935.

[99] X. Xie and A. Li, "Development of a topographic-corrected temperature and greenness model (TG) for improving GPP estimation over mountainous areas," *Agricult. Forest Meteorol.*, vol. 295, Dec. 2020, Art. no. 108193, doi: 10.1016/j.agrformet.2020.108193.

[100] T. R. McVicar, T. G. Van Niel, L. Li, M. F. Hutchinson, X. Mu, and Z. Liu, "Spatially distributing monthly reference evapotranspiration and pan evaporation considering topographic influences," *J. Hydrol.*, vol. 338, nos. 3–4, pp. 196–220, May 2007, doi: 10.1016/j.jhydrol.2007.02.018.

[101] K. Wang and R. E. Dickinson, "Contribution of solar radiation to decadal temperature variability over land," *Proc. Nat. Acad. Sci. USA*, vol. 110, no. 37, pp. 14877–14882, Sep. 2013, doi: 10.1073/pnas.1311433110.

[102] S. Pestana and J. D. Lundquist, "Evaluating GOES-16 ABI surface brightness temperature observation biases over the central sierra Nevada of California," *Remote Sens. Environ.*, vol. 281, Nov. 2022, Art. no. 113221, doi: 10.1016/j.rse.2022.113221.

[103] R. Pimentel, J. Herrero, and M. Polo, "Quantifying snow cover distribution in semiarid regions combining satellite and terrestrial imagery," *Remote Sens.*, vol. 9, no. 10, p. 995, Sep. 2017, doi: 10.3390/rs9100995.

[104] A. M. Wilson and W. Jetz, "Remotely sensed high-resolution global cloud dynamics for predicting ecosystem and biodiversity distributions," *PLOS Biol.*, vol. 14, no. 3, Mar. 2016, Art. no. e1002415, doi: 10.1371/journal.pbio.1002415.

Yichuan Ma received the B.S. degree from the University of Electronic Science and Technology of China (UESTC), Chengdu, China, in 2019. He is currently pursuing the Ph.D. degree with Wuhan University, Wuhan, China.

His main research interests include surface parameters estimation and energy budget in mountains.

Tao He (Senior Member, IEEE) received the B.E. degree in photogrammetry and remote sensing from Wuhan University, Wuhan, China, in 2006, and the Ph.D. degree in geography from the University of Maryland, College Park, MD, USA, in 2012.

He is currently a Professor with the School of Remote Sensing and Information Engineering, Wuhan University, and the Department of Geographical Sciences, University of Maryland. His research interests include surface anisotropy and albedo modeling, surface radiation budget, data fusion of satellite products, and long-term regional and global surface radiation budget analysis.

Cristina Aguilar was born in Spain in 1980. She received the B.Eng., M.Eng., and Ph.D. degrees from the University of Córdoba, Córdoba, Spain, in 2004, 2006, and 2008, respectively, all in hydrological engineering.

After a post-doctoral research position at the University of Granada, Granada, Spain, she joined the Department of Mechanics, University of Córdoba, as a tenured Associate Professor, in 2016. In recent years, she has focused on the stochastic characterization of dynamics systems with forecasting purposes. She has collaborated actively with researchers in several other disciplines of environmental and mechanical engineering. Her research interests lie in the area of hydrological processes and water quality modeling in semiarid environments.

Rafael Pimentel received the bachelor's degree in civil engineering from the University of Granada, Granada, Spain, in 2011, and the M.Eng. and Ph.D. degrees in hydrology from the University of Cordoba, Córdoba, Spain, in 2011 and 2014, respectively.

He has developed his career in the field of hydrology in mountainous semiarid regions. After his international experience at the Swedish Meteorological and Hydrological Institute, Norrköping, Sweden, he broadened his research to global hydrology, being one of the researchers involved in setting up of the World-Wide HYPE. Since September 2023, he has been an Assistant Professor at the University of Córdoba. He mainly researches snow dynamics by combining in situ and remote sensing information with physically based hydrological modelling in Mediterranean areas.

Shunlin Liang (Fellow, IEEE) received the Ph.D. degree from Boston University, Boston, MA, USA, in 1993.

He was a Faculty Member with the Department of Geographical Sciences, University of Maryland, College Park, MD, USA, for nearly 30 years. He is currently a Chair Professor and the Head of the Department of Geography, The University of Hong Kong, Hong Kong. He has published over 470 SCI indexed journal articles, 43 book chapters, and nine special issues of different journals. He authored/edited eight books and five of which were translated in Chinese, such as *Quantitative Remote Sensing of Land Surfaces* (Wiley, 2004), *Advances in Land Remote Sensing: System, Modeling, Inversion and Application* (Springer, 2008), *Advanced Remote Sensing: Terrestrial Information Extraction and Applications* (Academic Press, 2012 and 2019), *Global LAnd Surface Satellite (GLASS) Products: Algorithms, Validation and Analysis*(Springer, 2013), *Land Surface Observation, Modeling, Data Assimilation* (World Scientific, 2013), *Earth's Energy Budget* (Elsevier, 2017), and the *Geography of Contemporary China* (Spring, 2022). He has led to develop the multiple satellite products, including the GLASS products suite that is freely available (www.glass.umd.edu and www.geodata.cn) and has been widely used worldwide. According to Google Scholar, his H-index is 100, with the total citation of over 39 000. His main research interests focus on estimating essential environmental variables from satellite data, global high-level satellite product generation, Earth's energy balance, and environmental changes.

Dr. Liang was an Editor-in-Chief of the nine-volume books titled *Comprehensive Remote Sensing* (Elsevier, 2017) and an Associate Editor of IEEE TRANSACTIONS ON GEOSCIENCE AND REMOTE SENSING. He is an Editor-in-Chief of *Science of Remote Sensing*.

Tim R. McVicar is a remote sensing ecohydrologist with over 30-years research experience. He generates and uses remote sensing (mainly reflective and thermal) and gridded climate datasets to develop parsimonious models of ecosystem dynamics. He has been involved in numerous national and international projects and enjoyed working with other scientists to better understand water and vegetation dynamics. Seeing environmental managers make more informed decisions by using products, he codeveloped and helped policymakers incorporate new knowledge, and he cogenerated his ultimate work highlights. He is a Clarivate Highly Cited Researcher in 2021, 2022, and 2023 and has served our community via previously performing editorial roles with *Remote Sensing of Environment* and *Journal of Hydrology* and reviewing widely. His research is focused on understanding how climate changes, and other land-surface changes, impact vegetation, and water dynamics, so we can better manage these resources.

Dr. McVicar received the Chinese Academy of Sciences (CAS) President's International Fellowship Initiative (PIFI) Distinguished Scientist Award in 2020.

Dalei Hao received the B.S. degree in surveying and mapping engineering from Wuhan University, Wuhan, China, in 2015, and the Ph.D. degree from the Institute of Remote Sensing and Digital Earth, Chinese Academy of Sciences, Beijing, China, in 2020.

He is currently an Earth Scientist at the Pacific Northwest National Laboratory (PNNL), Richland, WA, USA. His research interests include land surface modeling, land–atmosphere interaction, and remote sensing.

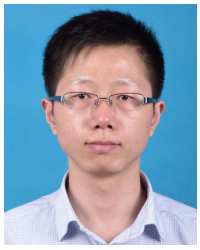

Xiongxin Xiao received the B.S. degree from the China University of Petroleum (East China), Qingdao, China, in 2015, the M.S. degree from Lanzhou University, Lanzhou, China, in 2018, and the Ph.D. degree from Wuhan University, Wuhan, China, in 2022.

He is currently a Post-Doctoral Fellow with the University of Bern, Bern, Switzerland. His research interests include snow remote sensing, data fusion, and climate change.

Xinyan Liu received the M.E. degree from the Shandong University of Science and Technology, Qingdao, China, in 2016, and the Ph.D. degree in photogrammetry and remote sensing from Wuhan University, Wuhan, China, in 2023.

She is currently a Research Assistant with the Aerospace information institute, Henan Academy of Sciences, Zhengzhou, China. Her research interests include interaction between cloud and radiative parameters, data fusion of satellite products, and long-term regional surface radiation budget, especially in the Arctic region.